Climate
of the Past

Simulating glacial dust changes in the Southern Hemisphere using ECHAM6.3-HAM2.3

Stephan Krätschmer[1], Michèlle van der Does[1], Frank Lamy[1], Gerrit Lohmann[1,2], Christoph Völker[1], and Martin Werner[1]

[1]Alfred Wegener Institute, Helmholtz Centre for Polar and Marine Research, Bremerhaven, Germany
[2]Physics Department, University of Bremen, Bremen, Germany

Correspondence: Stephan Krätschmer (stephan.kraetschmer@awi.de)

Abstract. Mineral dust aerosol constitutes an important component of the Earth's climate system, not only on short timescales due to direct and indirect influences on the radiation budget but also on long timescales by acting as a fertilizer for the biosphere and thus affecting the global carbon cycle. For a quantitative assessment of its impact on the global climate, state-of-the-art atmospheric and aerosol models can be utilized. In this study, we use the ECHAM6.3-HAM2.3 model to perform global simulations of the mineral dust cycle for present-day (PD), pre-industrial (PI), and last glacial maximum (LGM) climate conditions. The intercomparison with marine sediment and ice core data, as well as other modeling studies, shows that the obtained annual dust emissions of 1221, 923, and 5159 Tg for PD, PI, and LGM, respectively, generally agree well with previous findings. Our analyses focusing on the Southern Hemisphere suggest that over 90 % of the mineral dust deposited over Antarctica are of Australian or South American origin during both PI and LGM. However, contrary to previous studies, we find that Australia contributes a higher proportion during the LGM, which is mainly caused by changes in the precipitation patterns. Obtained increased particle radii during the LGM can be traced back to increased sulfate condensation on the particle surfaces as a consequence of longer particle lifetimes. The meridional transport of mineral dust from its source regions to the South Pole takes place at different altitudes depending on the grain size of the dust particles. We find a trend of generally lower transport heights during the LGM compared to PI as a consequence of reduced convection due to colder surfaces, indicating a vertically less extensive Polar cell.

1 Introduction

In the last few decades, mineral dust has been identified as playing an important role in the climate system due to its various interactions in atmospheric processes (e.g., Maher et al., 2010). The emission of dust particles takes place in arid and semi-arid areas and is controlled by several meteorological factors and surface properties in the source areas, for instance, wind speed, soil moisture, the type and amount of vegetation, soil composition, and the occurrence of other non-erodible elements (Goudie, 2008). Once suspended, especially smaller dust particles can get transported over large distances and distributed by the global atmospheric circulation before they are removed from the atmosphere by sedimentation, turbulent deposition, or scavenging. During transport, the dust particles directly influence Earth's radiation budget by scattering and absorbing shortwave and longwave radiation depending on particle size and mineralogical composition (Dufresne et al., 2002; Balkanski et al., 2007), which in turn affects the atmospheric stability by altering the vertical temperature profile and relative humidity (Boucher, 2015). Besides these direct effects on the energy budget, mineral dust particles act as cloud condensation and ice nuclei and thus affect optical and other microphysical properties of clouds, which again influences the radiation budget (Spracklen et al., 2008).

However, the role of mineral dust in the Earth system is by no means limited solely to the radiative energy balance. Depending on the mineralogical composition of the dust particles, they may constitute a very important source of micronutrients for some ecosystems. By acting as a fertilizer

for the vegetation and the biosphere in general, mineral dust also plays a crucial role in the carbon cycle and its impact on the global climate. Saharan dust, for instance, has been identified to represent an important source of phosphorus for the Amazon rainforest, where the soil shows a general depletion (Reichholf, 1986). Another example for an ecosystem depending on the fertilizing effects of dust is the Southern Ocean. Onboard incubation experiments showed that the bioproductivity in this region is strictly limited by iron availability (Martin et al., 1990). Based on the results of these experiments, Martin (1990) proposed the so-called iron hypothesis, which states that increased amounts of bioavailable iron were supplied during glacials in that region by enhanced mineral dust deposition. As a consequence of the atmospheric iron input, phytoplankton blooms emerged, binding huge amounts of CO_2. After death, large parts of the organic matter sunk down into the deep sea, effectively removing the bound CO_2 from the atmosphere and thus contributing significantly to the observed reduction from 280 ppm to well below 200 ppm CO_2 during the last glacial period. Estimates based on paleoceanographic data constrain the upper limit of this effect to 40 ppm, since increased aeolian dust fluxes are only observed once the atmospheric CO_2 concentration had already decreased by 40 to 50 ppm (Martínez-Garcia et al., 2011).

The analysis of ice cores and marine sediments from both hemispheres has provided detailed data on the spatial and temporal variability of dust deposition fluxes, both in total amount and particle size distribution, over the last million years on a global scale and has enabled the utilization of mineral dust as a climate proxy. However, the interpretation of these data turns out to be quite challenging due to their multifactorial causes. For instance, it has not yet been finally resolved whether climatic changes in the source regions (e.g., soil moisture, wind speed, vegetation cover) or changes in the atmosphere (e.g., wind speed, circulation patterns, particle lifetime) were the primary driver causing up to 20 times higher dust fluxes to Antarctica during glacials (Kohfeld and Ridgwell, 2009; Wolff et al., 2010). The situation is similar with the data on particle sizes. Ice core data from Greenland, for instance, show the deposition of significantly coarser dust during cold climates (Steffensen, 1997), which has been interpreted as a consequence of stronger winds transporting coarser particles over larger distances or as a result of the appearance of a closer dust source not active during warmer climates (Mahowald et al., 2014). Contrastingly, ice core data from Antarctica indicate the deposition of generally finer particles during glacials, although a regional analysis reveals the deposition of slightly coarser particles in parts of central East Antarctica (Delmonte et al., 2002, 2004). The regional difference is explained by changes in the atmospheric circulation leading to dust transport pathways of different lengths from the sources to the deposition areas. On longer trajectories, a larger proportion of coarser particles gets removed during transport, and the observed particle size distribution in the deposition area is consequently shifted to finer particles. In

order to support or reject such a hypothesis, the unambiguous identification of the dust's provenance is indispensable. Based on measurements of strontium (Sr) and neodymium (Nd) isotope ratios, southern South America has been identified as the most likely source of dust found in Antarctic ice cores that has been delivered during the last glacial (Basile et al., 1997). This finding has been supported by the study of Lunt and Valdes (2002), who found via a back-trajectory modeling approach that "[mineral dust] transport from Patagonia [to Antarctica] is much more efficient than transport from both Australia and South Africa", which the authors explain by the southward extension of Patagonia well into "the strong winds over the Southern Ocean". However, it is still challenging to identify minor source contributions in the presence of a predominant dust source (Vallelonga, 2014). For instance, the characteristic isotope ratios of $^{87}Sr/^{86}Sr$ and $^{143}Nd/^{144}Nd$ of mineral dust found in Antarctic ice cores and delivered during interglacials match not only those of southern South American soil samples but also the ratio of soil samples from central and southeastern Australia (De Deckker et al., 2010). This finding suggests that transport of Australian dust to Antarctica is generally possible and raises the question if and to what degree Australian dust sources might also have contributed to the total amount of dust found in ice cores during glacials and which climate elements caused the according changes.

In this study, we use a state-of-the-art atmospheric general circulation model coupled to an aerosol model in order to provide new global simulations of the dust cycle for different climate conditions. We compare our present-day simulations to results obtained in the scope of the global dust model intercomparison in AeroCom phase I in order to assess the performance of our model. The main focus of our study is, however, a comprehensive and quantitative characterization of the global dust cycle during the last glacial maximum (LGM, 21 ka), in particular compared to the pre-industrial (PI, 1850–1879 CE) dust cycle. In order to verify our simulation results, we use observational data for a detailed comparison. Our provenance studies focus on the Southern Hemisphere and give new insights on the respective contribution of the three major dust source regions, Australia, South Africa, and Patagonia, to the total dust deposition in the Southern Hemisphere. Finally, we use the combined global and local information on particle sizes and lifetimes, as well as precipitation and wind patterns, to draw conclusions concerning the atmospheric circulation in the Southern Hemisphere during the LGM.

2   Model description

In this section, a concise overview on the model ECHAM-HAMMOZ used in our study is given. It consists of the atmospheric circulation model ECHAM6.3 coupled to the aerosol model HAM2.3 as well as the model for atmospheric gas-

phase chemistry MOZ1.0. The sub-models HAM and MOZ can both be independently switched on and off. In the scope of our study, we only run the aerosol model and use monthly prescribed oxidant fields. A detailed description of the complete model is given in Schultz et al. (2018).

2.1 Atmospheric general circulation model ECHAM6.3

ECHAM6 (subversion ECHAM6.3.02 in this study) is the latest version of an atmospheric general circulation model developed by the Max-Planck Institute in Hamburg (Stevens et al., 2013). In the late 1980s, it was branched from a model used at the European Center for Medium Range Weather Forecasts (ECMWF). Since then, new numerical schemes and physical processes have been included and released with each upcoming new model version. The model code can be roughly divided into two parts, one consisting of the adiabatic core and the other consisting of a suite of physical parameterizations for diabatic processes on the sub-grid scale.

The adiabatic core uses a mixed finite-difference and spectral-discretization approach to solve the according primitive equations for the hydrodynamic variables vorticity and divergence and the thermodynamic variables temperature and surface pressure. A spectral-transform method is used to represent horizontal spatial differences (Simmons et al., 1989), applying a triangular truncation using a finite number of modes (e.g., T63). In the vertical, the model is discretized by either 47 or 95 model layers (L47 or L95) on a Lorenz grid up to a model top of 0.01 hPa, corresponding to a height of about 80 km. The implemented numerical scheme for vertical advection conserves potential and kinetic energy; pressure gradients are calculated by a scheme conserving angular momentum (Simmons and Jiabin, 1991). For tracer transport, a flux-form semi-Lagrangian scheme on a Gaussian grid is used due to its inherent conservation properties (Lin and Rood, 1996).

As mentioned above, ECHAM6 comes with a comprehensive set of parameterizations. The boundary layer and turbulence are parameterized based on an eddy diffusivity approach (Brinkop and Roeckner, 1995). The model generally allows for shallow, mid-level and deep convection, although only one type of convection is allowed per grid cell, with a preference for deep convection. Convective clouds and their according transport are calculated by a mass-flux scheme. The sub-grid orography is parameterized according to Lott (1999) in order to account for momentum transport in the boundary layer and gravity waves. Sub-grid-scale cloudiness is determined by calculating the cloud fraction based on the relative humidity once a threshold value is exceeded (Sundqvist et al., 1989). While the cloud droplet number concentration is only parameterized depending on the altitude in the base model version of ECHAM6, the coupling to the aerosol model HAM2.3 now enables an explicit calculation based on aerosol activation (see Sect. 2.2). The transport of cloud water and ice is prognostically calculated, accounting for adiabatic circulations, phase transitions, and the conversion to large-scale precipitation (Lohmann and Roeckner, 1996). Radiative transfer is parameterized by dividing the relevant part of the electromagnetic spectrum into 14 shortwave and 16 longwave bands, and absorption is calculated over all bands depending on trace gas concentrations and ambient pressure using look-up tables. The optical properties of clouds for each band are calculated based on Mie theory; for aerosols the according treatment is described in Sect. 2.2. A novelty that came up with ECHAM6 is the integration of the land surface and vegetation model JSBACH (Reick et al., 2013). Therein, each grid cell is assumed to be tiled allowing various shares of bare soil and 12 different plant functional types, whereas the soil hydrology is represented by a five-layer scheme (Hagemann and Stacke, 2015). The sub-model allows for the calculation of dynamic vegetation and provides physical parameters like evaporation and surface albedo.

2.2 Aerosol model HAM2.3

In this subsection, a brief overview on the Hamburg Aerosol Model (HAM) is given. Essentially, it constitutes a comprehensive microphysics package taking into account all relevant processes and interactions of the five atmospheric aerosol species sulfate, black carbon, organic carbon, sea salt, and mineral dust. The very first version was developed and coupled to ECHAM5 by Stier et al. (2005). Since then, it has been extended several times by new numerical schemes and considered processes and coupled to the latest ECHAM release (Tegen et al., 2019; Neubauer et al., 2019).

2.2.1 General overview

Similar to ECHAM6.3, HAM2.3 can also be roughly split up into two parts, with one mainly treating large-scale processes like emission, transport, and deposition of aerosol particles, while the other deals with the microphysical processes, such as nucleation, condensation, coagulation, and hydration. For the latter, the default sub-model in HAM2.3 is the modal M7 aerosol model (Vignati et al., 2004), which represents the particle size distribution via seven superimposed log-normal modes and is also used in our study.

The seven log-normal modes in M7 consist of four soluble and three insoluble modes, representing the nucleation mode (number median radius $\bar{r} < 5$ nm, only soluble mode), Aitken mode (5 nm $< \bar{r} < 50$ nm), accumulation mode (50 nm $< \bar{r} < 500$ nm), and coarse mode ($\bar{r} > 500$ nm). Hereby, the soluble modes are assumed to be perfectly internally mixed. Each mode is mathematically defined by three moments of the distribution, namely the aerosol number N, the number median radius $\bar{r}$, and the standard deviation σ. The latter is set to $\sigma = 1.59$ for the nucleation, Aitken, and accumulation modes and $\sigma = 2.00$ for the coarse modes (Wilson et al., 2001). In each time step, HAM calculates the transport of the tracer aerosol mass and aerosol number. Sub-

sequently, the number median radius $\bar{r}$ can be determined for each mode and grid cell based on the given information. Each mode is consequently confined by the boundaries given above, though the number median radius changes over time due to various processes transferring particles between modes, respectively, removing or adding particles from or to modes. All further size-dependent processes are calculated based on this number median radius for all particles of a specific mode. Aerosol particles devolve from insoluble to soluble modes either due to condensation of sulfate on their surface or due to coagulation with particles of soluble modes. The aerosol dynamics are based on a general coagulation equation, calculating the change in the particle number for each mode and time step considering inter- and intra-modal coagulation, as well as sources and sinks. Interactions between aerosol particles and clouds are parameterized by an explicit activation scheme based on Köhler theory (Abdul-Razzak and Ghan, 2000). As mentioned above, HAM enables the explicit calculation of cloud droplet and ice crystal number concentrations, which is done via a two-moment cloud microphysics scheme (Lohmann et al., 2007; Lohmann and Hoose, 2009). The optical properties of the aerosols are not calculated online in order to save on computational costs. Instead, a look-up table provides pre-calculated values based on Mie theory and contains the Mie size parameter and the real and imaginary part of the refractive index. Aerosols and aerosol precursor are emitted from various natural (biosphere, ocean, etc.) and anthropogenic sectors (industry, ships, power plants, etc.), where natural emissions are calculated online while emissions from anthropogenic sectors are provided in form of external input fields (see Sect. 2.2.3). Considered particle removal processes include dry deposition, sedimentation based on a Stokes settling velocity approach, and particle-size-dependent in- and below-cloud scavenging (Croft et al., 2009, 2010).

2.2.2   Treatment of mineral dust in HAM2.3

Of particular importance in the scope of this study is the treatment of mineral dust aerosol in HAM2.3. Since dust is only emitted from arid and semi-arid areas without vegetation or covered only by low vegetation, the determination of those regions is a crucial point in order to attain a suitable parameterization of the dust emission process. We use a scheme introduced by Stanelle et al. (2014), which enables a fully interactive coupling between JSBACH and ECHAM6 with respect to dust emissions and was developed in order to investigate the impact of anthropogenic land use change on the global dust cycle. Hereby, terrestrial tiles not covered by any vegetation represent potential dust source areas, whereas tiles covered by snow or vegetation block dust emissions. While gaps in low-stature vegetation such as shrubs and crops allow for dust emissions, gaps in forests prevent them. The direct coupling of the dust emissions to the land surface and vegetation model automatically accounts for any changes, for

instance in the land–sea distribution as a consequence of past climate changes.

The dust emission process is parameterized based on the wind speed at 10 m elevation. In order to determine the total emission flux, particles of all soil types are divided into 192 dust size bins ranging from 0.2 to 1300 μm, and a threshold friction velocity is calculated individually for each bin (Marticorena et al., 1997). The calculation of the saltation process is based on an explicit formulation of Marticorena and Bergametti (1995). Since water increases the cohesive forces among dust particles, dust emission is prohibited once the soil moisture of the uppermost layer exceeds a threshold value. In all dust source regions, a constant surface roughness length of 0.001 cm is prescribed. The vertical dust emission flux is finally calculated based on the horizontal dust flux according to White (1979), whereas the particles are emitted either into the insoluble accumulation mode (mass median radius (mmr) = 0.37 μm, $\sigma = 1.59$) or the insoluble coarse mode (mmr = 1.75 μm, $\sigma = 2.00$). Due to their short lifetimes, emissions into the super-coarse mode are neglected (Stier et al., 2005; Cheng et al., 2008). Since the surface orography is not taken into account in ECHAM6.3 in order to determine the aerodynamic surface roughness length, so-called regional correction factors are applied on the threshold friction velocity to account for "subsequent changes in surface wind distributions over dust source areas" (Tegen et al., 2019). They can be set for each dust source region individually and are chosen such that the simulated emissions match best with values by Huneeus et al. (2011). We also use those factors in the scope of our study to switch specific dust source areas on and off individually for the according experiments.

2.2.3   Simulation setup and experiments

We perform global simulations for present-day (PD, 1996–2005 CE), pre-industrial (PI, 1850–1880 CE) and last glacial maximum (LGM, 21 ka) climate conditions using the spatial resolution T63 (1.875° × 1.875°) with 47 vertical layers. While an initial run ("cold start") is performed for PD and PI, the model is initialized by restart files for the LGM, which represent a dynamic equilibrium of the model obtained after several hundred simulation years for the according topographic, vegetation, and climate conditions. The spin-up time is 10 years for PD and PI and 20 years for the LGM, and the total simulation period is 20 years for PD, 40 years for PI, and 50 years for LGM. Except for PD, the final 30 simulation years are evaluated in order to calculate mean values. Our simulation setup consists of an atmosphere-only model, i.e., our model is not coupled to an ocean model. Instead, we provide the boundary conditions for the sea surface temperature and the sea ice concentration in form of monthly resolved input files. For PD, we use monthly resolved 30-year means for the years 1979–2008 based on the Atmospheric Model Intercomparison Project – Phase II (AMIP II) dataset (Taylor et al., 2000), for PI we prescribe monthly resolved

30-year means for the years 1870–1899 created in the scope of the Program for Climate Model Diagnosis and Intercomparison (PCMDI) based on the latest AMIP II dataset (Durack and Taylor, 2019), and for the LGM we use monthly resolved 30-year means based on reconstructions in the scope of the Glacial Atlantic Ocean Mapping (GLAMAP, Paul and Schäfer-Neth, 2003). The emission of aerosols and aerosol precursor from various anthropogenic sectors (see Schultz et al., 2018) for PI and PD are prescribed in form of monthly resolved input files based on the Atmospheric Chemistry and Climate Model Intercomparison Project (ACCMIP) dataset (Lamarque et al., 2010). For LGM runs, greenhouse gas concentrations and orbital parameters have been set in accordance with the Paleoclimate Model Intercomparison Project – Phase 4 (PMIP4) experimental setup (Kageyama et al., 2017). Since a large amount of water was bound in ice sheets covering large parts of North America and northern Europe during the LGM, the land–sea mask has also been updated accordingly in order to account for a 125 m lower sea level compared to present-day conditions (e.g., Clark et al., 2009). In all simulations, dynamic vegetation is calculated online by JSBACH. It should be mentioned that the JSBACH restart files used for the LGM run initialize a desert in a small region on the northeastern coast of South America. Although efforts to reconstruct the vegetation in the Amazon region indeed show a patch-like retreat of the rainforest during the LGM, the surrounding vegetation is instead suggested to have consisted of tropical grassland instead of a desert (e.g., Ray and Adams, 2001). Consequently, we prohibit dust emissions in this region and accept this small shortcoming of the land surface and vegetation model.

3 Results and discussion

3.1 Model performance for present-day climate conditions

The present-day simulation is intended to evaluate the model's performance concerning the representation of the global dust cycle. Table 1 shows a comparison of several key values used to characterize the global dust cycle budget of our modeling results in relation to the global dust model intercomparison in AeroCom phase I for present-day climate conditions (Huneeus et al., 2011). In terms of total annual dust emissions, our model simulates $1221\,\mathrm{Tg\,yr^{-1}}$, which is close to the AeroCom median values of $1123\,\mathrm{Tg\,yr^{-1}}$. Generally, our model performs at the lower end of the 1000–$4000\,\mathrm{Tg\,yr^{-1}}$ range of dust emissions estimated by the IPCC (Intergovernmental Panel on Climate Change, 2014), which is caused by the neglect of a super-coarse particle mode (Stanelle et al., 2014). As a consequence of the comparably small particle sizes, the simulated atmospheric dust burden of 19.8 Tg is slightly higher than the AeroCom median of 15.8 Tg, which also leads to a higher averaged particle lifetime of 5.96 d compared to the 4.59 d for the AeroCom

median. A noticeable difference is also the respective contribution of the three different deposition mechanisms, wet deposition, dry deposition, and sedimentation. While the AeroCom median suggests an almost equal proportion of 357, 396, and $314\,\mathrm{Tg\,yr^{-1}}$, respectively, the most dominant deposition mechanism in our model is wet deposition, with $708\,\mathrm{Tg\,yr^{-1}}$, followed by sedimentation ($412\,\mathrm{Tg\,yr^{-1}}$), and finally dry deposition ($93\,\mathrm{Tg\,yr^{-1}}$). Again, this can be explained with the comparably small particle sizes: dry deposition and sedimentation apply first and foremost to larger particles close to the source regions, while rain scavenging is the predominant deposition mechanism in remote areas after long-range transport, which mostly applies to smaller particles in particular. Based on this intercomparison we conclude that the model setup used in our study represents the global dust cycle adequately for the following investigations. A comparison of the simulated total dust deposition with observational data from 84 sites provided by Huneeus et al. (2011) can be found in the Supplement (Figs. S1 and S2).

3.2 The dust cycle under pre-industrial and last glacial maximum climate conditions

3.2.1 Overview

Figure 1 shows the results concerning the global dust cycle for PI and the LGM. We find an annual global dust emission of 923 and $5159\,\mathrm{Tg\,yr^{-1}}$ for PI and the LGM, respectively. Our model identifies northern Africa and Asia as major dust source regions in the Northern Hemisphere and southern South America, southern Africa, and Australia as major dust source regions in the Southern Hemisphere (Fig. 1a and b). The zonally averaged dust emissions shown in Fig. 1c reveal that while all sources emit noticeably more dust during the LGM compared to PI, the increase is most significant for Asia, northern Africa, and Australia. As a consequence of the higher dust emissions during the LGM, the dust burden also increases from 16 to 99 Tg. Once emitted, the dust is distributed by the atmospheric circulation (Fig. 1d and e). The northeasterly and southeasterly trade winds transport in particular northern and southern African dust along the Equator over the Atlantic Ocean, while dust emitted in Asia and southern South America (and Australia) gets transported by the westerlies over the Pacific Ocean and the Southern Ocean, respectively. Finally, the dust deposition patterns naturally follow the dust burden patterns (Fig. 1g and h). As expected, the depositions in midlatitudes close to the source regions are higher during the LGM (Fig. 1i). However, it should be noted that in remote regions in both hemispheres more dust deposition also occurs, particularly in the high latitudes. Our model simulates a deposition of $423\,\mathrm{Tg\,yr^{-1}}$ (45 %) and $2122\,\mathrm{Tg\,yr^{-1}}$ (41 %) onto the oceans globally for PI and the LGM.

Table 1. Comparison of key values characterizing the global dust cycle budget between the model used in this study, ECHAM6.3-HAM2.3, and the AeroCom median resulting from an intercomparison of 14 different atmosphere models for present-day climate conditions (Huneeus et al., 2011).

Model/experiment	Emission [Tg yr^{-1}]	Burden [Tg]	Deposition [Tg yr^{-1}]	Wet deposition [Tg yr^{-1}]	Dry deposition [Tg yr^{-1}]	Sedimentation [Tg yr^{-1}]
ECHAM6.3-HAM2.3 decadal mean 1996–2005	1221	19.8	1213	708	93	412
AeroCom median for year 2000 (range)	1123 (514–4313)	15.8 (6.8–29.5)	1257 (676–4359)	357 (295–1382)	396 (37–2791)	314 (22–2475)
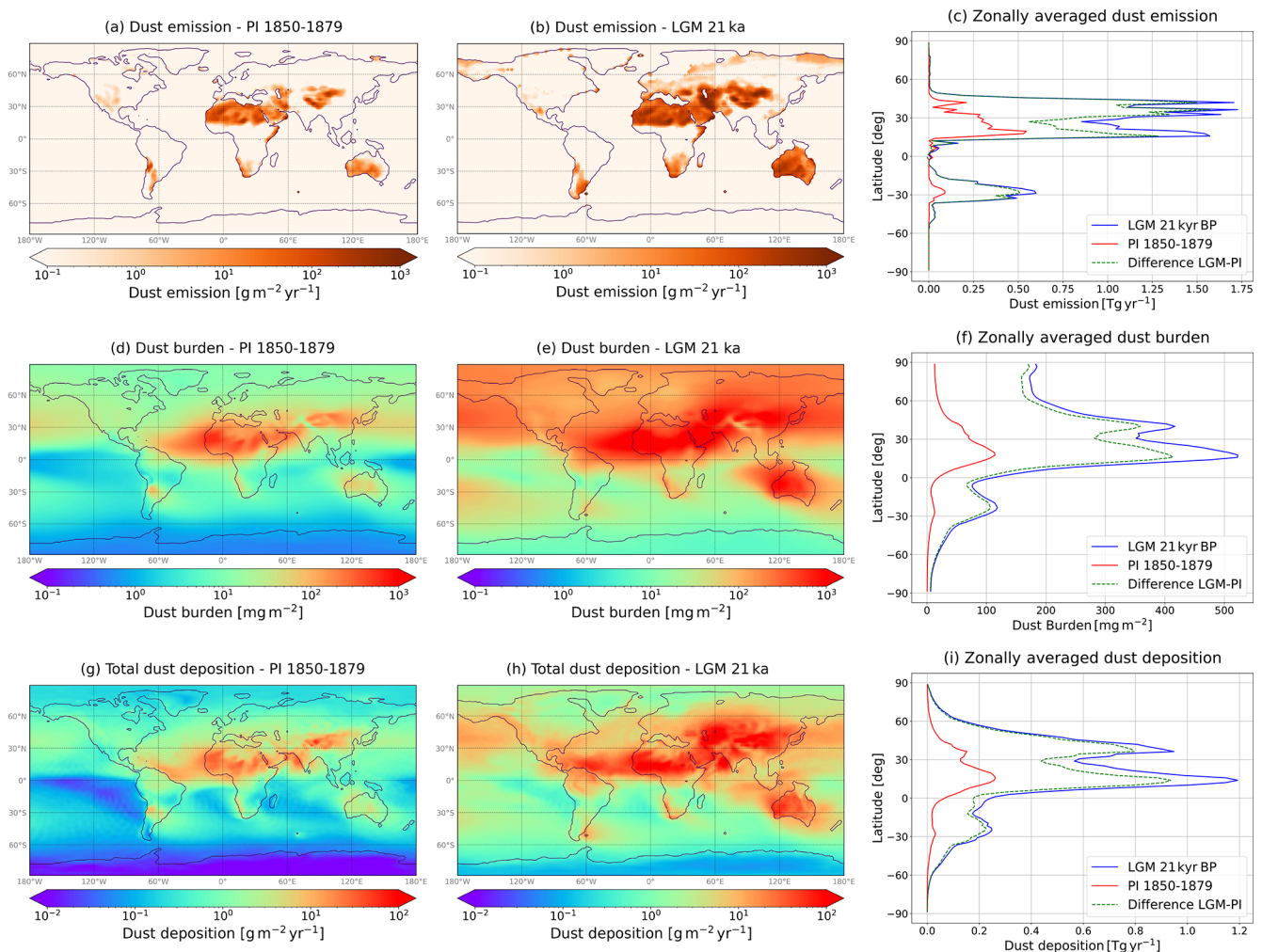
Figure 1. Global maps showing the dust emission, burden and deposition for PI (**a, d, g**) and LGM climate conditions (**b, e, h**). Additionally, zonally averaged graphs are shown for all quantities (**c, f, i**).

With respect to dust emissions, our values are lower than the simulated 2785 Tg yr^{-1} for PI and 6294 Tg yr^{-1} for the LGM of the Community Earth System Model (CESM) (Albani and Mahowald, 2019), whereas the differences are more significant for PI (Table 2). The major dust source regions we identified for both the Northern Hemisphere and the Southern

Hemisphere are in accordance with other studies (e.g., Takemura et al., 2009), suggesting that the interactive coupling of dust emissions to the land surface and vegetation model JS-BACH in our model yields reliable results (see Table 3 for detailed regional values). As a consequence of the atmospheric circulation pattern, the increased zonally averaged dust bur-

den in the high northern latitudes during the LGM (Fig. 1f) can at least partly be attributed to the markedly higher dust emissions in Asia compared to PI, which is in accordance with results by Werner et al. (2002). With respect to dust deposition, our model simulates a higher relative proportion of dust deposited over the oceans than the 440 Tg yr^{-1} (16 %) for PI and the 826 Tg yr^{-1} (13 %) for LGM found by Albani et al. (2016) using CESM. Shao et al. (2011) evaluated results of several modeling studies and found on average a dust emission of 2000 Tg yr^{-1}, of which 25 % deposit over the oceans. Regardless of the differences in absolute numbers it is worth noting that both models indicate a decreased deposition proportion for LGM climate conditions. However, it is possible that our prescribed SSTs are too warm (Tierney et al., 2020). While our study does not indicate a suggested equatorward shift of the westerlies, other studies have shown an influence of prescribed SSTs and SIC on the westerlies (e.g., Sime et al., 2013).

Based on the previous findings, it can be concluded that the differences of ECHAM6.3-HAM2.3 in comparison to CESM in terms of dust modeling can be traced back to the modeled particle size distribution. The atmospheric component of CESM, CAM4, utilizes a sectional approach in order to represent the particle size distribution, grouping the particles into four size bins ranging from 0.1 to 10 µm in diameter (Mahowald et al., 2006). The higher dust emission fluxes in CESM, in particular for PI climate conditions, are consequently caused by larger particles, which add to the mass budget significantly, and their rapid sedimentation close to the source regions lowers the average particle lifetime (Albani et al., 2014). The smaller particle sizes modeled by ECHAM6.3-HAM2.3, however, enable long-range transport to remote regions for a large proportion of the emitted dust and consequently causes wet scavenging to become the predominant deposition mechanism. The importance of an adequate modeling of finer dust in order to achieve a proper representation of long-range transport and subsequent deposition over the oceans has already been pointed out by Mahowald et al. (2014). In the end, the question as to how well our model performs in absolute values can only be evaluated by comparing the results to measurement data, which is done in Sect. 3.2.2.

On average 5.6 times higher dust emissions are simulated for LGM compared to PI climate conditions (Table 3). While the increase is only 5.3-fold in the Northern Hemisphere, the ratio is even 9.8 for the Southern Hemisphere. This raises a question concerning the causes of this significant increase. One obvious reason is the difference in the land–sea distribution, as can be seen in Fig. 1. Globally, the extended drylands during the LGM in the coastal regions as a consequence of the lower sea level, for instance in South America and Australia (Fig. 1a and b), emit 229 Tg yr^{-1} of mineral dust and thus contribute only around 5 % to the total increase. On a regional scale, the extended drylands contribute around 13 % in Australia and 10 % in southern Africa to the increased dust

emissions. Only in southern South America, does more than 80 % of the increased dust emissions during the LGM come from the extended drylands (see Table 4). However, dust emissions also depend on meteorological factors like wind speed and soil moisture. Figure 2 shows anomalies (LGM – PI) with respect to the 2 m temperature, annual precipitation, and 10 m wind speed. The ice sheet over North America and northern Europe caused a significant temperature drop in the corresponding regions during the LGM (Fig. 2a), while the decrease around the Equator was less pronounced, which resulted in a globally averaged lower temperature of −4.1 °C. The steeper temperature gradient between high latitudes and the Equator during the LGM (Fig. 2b) caused noticeably stronger winds in the Northern Hemisphere (Fig. 2e and f), and the generally colder climate resulted in a precipitation decline at the Equator and close to the poles (Fig. 2c and d), averaging to a global anomaly of −6.8 cm yr^{-1}. Since precipitation acts as an effective deposition mechanism, the drier climate north of 45° N also contributes to the higher dust burden towards the North Pole as a result of the increased particle lifetime in addition to the higher dust emissions in Asia (Fig. 1f). In the Northern Hemisphere the wind speed anomaly averages to +0.49 m s^{-1}, and Fig. 2e reveals that there was an increase over the major dust source regions of Asia and northern Africa. Although the zonally averaged wind speed in Fig. 2f suggests no significant differences between LGM and the PI in the Southern Hemisphere (+0.04 m s^{-1}), the map shown in Fig. 2e indicates considerable differences over the major Southern Hemisphere dust source regions. A regional analysis yields a 10 m wind speed anomaly of +0.77 m s^{-1} over Australia, +0.44 m s^{-1} over southern Africa, and +0.52 m s^{-1} over Patagonia. With respect to precipitation, the model simulates a decrease of −31.7 cm yr^{-1} for Australia and −28.2 cm yr^{-1} for southern Africa and a slight increase of +7.1 cm yr^{-1} for Patagonia (Fig. 2c). These findings are in agreement with results by Rojas et al. (2009), who found in the scope of the PMIP2 simulations a generally colder, drier climate south of 40° S but slightly more precipitation over Patagonia during the LGM. Finally, the dust emissions also depend on the vegetation cover. As can be seen in Fig. 2g and h, arid and semi-arid areas were substantially further extended during the LGM compared to PI, particularly in Asia, Australia, southern Africa, and Patagonia.

Based on our findings, we conclude that the increase in dust emissions during the LGM compared to the PI was caused by extended drylands in the source regions and at the coasts due to a lower sea level, reduced vegetation cover, regionally increased wind speeds, and less precipitation over the source regions, which is also in agreement with findings by Lunt and Valdes (2002).

Table 2. Key values for dust emission, burden, and deposition characterizing the global dust cycle budget as simulated by our model ECHAM6.3-HAM2.3 compared to results obtained with CESM (Albani and Mahowald, 2019).

Model/experiment	Emission [Tg yr^{-1}]	Burden [Tg]	Deposition [Tg yr^{-1}]	Wet deposition [Tg yr^{-1}]	Dry deposition [Tg yr^{-1}]	Sedimentation [Tg yr^{-1}]
ECHAM6.3-HAM2.3 30-year mean PI 1850–1879	923	16	929	547	57	325
CESM PI year 1850	2785	20	–	–	–	–
ECHAM6.3-HAM2.3 30-year mean LGM 21 ka	5159	99	5171	3096	473	1602
CESM LGM 21 ka	6294	37	–	–	–	–

Table 3. Global and regional dust emissions during the PI and LGM in Tg yr^{-1} and the LGM/PI ratio.

Emission [Tg yr^{-1}]	PI 1850–1879	LGM 21 ka	LGM/PI ratio
Globally	923	5159	5.6
Northern Hemisphere	835 (90.6 %)	4300 (83.3 %)	5.3
Southern Hemisphere	88 (9.4 %)	859 (16.7 %)	9.8
Sahara	535	1626	3
Arabian Peninsula	70	430	6.1
Asia	204	1803	8.8
Australia	47	748	15.9
Southern Africa	12	63	5.3
Patagonia	2.3	36	15.6

3.2.2   Comparison to observational data

We use the compilation of dust deposition data from Kohfeld et al. (2013) for a comparison between our simulated dust deposition in the Southern Hemisphere and data based on marine sediment and ice core analysis.

Figure 3 shows dust deposition maps including observations and scatter plots comparing simulated and measured dust deposition for the PI, LGM, and the LGM/PI ratio. For a more differentiated analysis, the data points have been categorized into five groups according to their geographical region. For both PI and the LGM, the simulated values are mostly in accordance with the observed values for the Atlantic Ocean (Fig. 3b and d, blue diamonds). Due to the atmospheric circulation, dust deposited in the region close to the Equator originates mainly from the Sahara and southern Africa, whereas dust deposited in the southern Atlantic Ocean is mainly of southern South American origin. The model reveals a tendency to underestimate the depositions over the Pacific Ocean and Pacific Southern Ocean, particularly in the PI simulation (Fig. 3b and d, green circles and triangles), as well as a systematic overestimation of the dust depositions onto Antarctica (Fig. 3b and d, orange pentagons) by and order of magnitude. At least for the Pacific region,

Australia can be assumed to be the major source, which indicates that the model simulates too low dust emissions. However, the dust deposited over the Tasman Sea is also very likely of Australian origin (Fig. 3b and d, red crosses). While the simulation values are in good accordance with the observations in that region for PI, the model overestimates the dust deposition during the LGM. Figure 3e and f show a comparison between the simulated dust deposition ratios LGM/PI and the measurement values, suggesting that this ratio varies strongly on a regional scale. For instance, our simulation results indicate a 5-fold to 40-fold increase in dust deposition over Antarctica, whereas a 1-fold to 4-fold increase has been simulated over the Atlantic (Fig. 3f).

As our analyses of dust provenance (Sect. 3.2.3) reveal, the dust deposition over Antarctica is dominated by the Australian contribution during the LGM. Thus, the comparison of our model results with the observational data showing lower simulated values in the Pacific Ocean and Pacific Southern Ocean gives no clear hint as to whether Australia's source strength is overestimated or underestimated in the model. A possible factor contributing to this inconsistency could be a too high transport efficiency of dust towards the South Pole. However, considering the difference in absolute values between dust deposition over the Pacific Ocean and

Table 4. Additional land areas in Australia, southern Africa, Patagonia, and globally during the LGM compared to the PI due to the lower sea level in 10^6 km^2 and the dust emissions from those extended drylands (in Tg yr^{-1}).

	Additional land area LGM [10^6 km^2]	Dust emission [Tg yr^{-1}] PI 1850–1879	Dust emission [Tg yr^{-1}] LGM 21 ka	Dust emission [Tg yr^{-1}] from additional land areas
Globally	19.5	923	5159	229
Australia	1.8	47	748	92
Southern Africa	0.04	12	63	5
Patagonia	0.8	2.3	36	29

Antarctica, which is almost 3 orders of magnitude, a too high transport efficiency can be excluded as the sole reason for the discrepancies. Another factor that needs to be considered are non-aeolian contributions. Although data from "marine sites that have been flagged because they are located within zones of thick nepheloid layers and ice-rafted detritus, which can contaminate aeolian signals" had already been excluded from the dataset we use for comparison (Kohfeld et al., 2013), the reconstructed detrital flux estimates might still contain contributions from glacier erosion and riverine input, which are not considered in our model. The dust flux reconstructions are based on the assumption of relatively constant proportions of ^{232}Th in continental lithogenic materials and might thus be overestimated by 30 %–40 % in regions receiving fine-grained dust from Patagonia and Australia since fine sediments have "a reduced proportion of low-^{232}Th phases such as quartz and feldspar" (McGee et al., 2015). The lack of non-aeolian contributions in our model might also contribute to the fact that the simulated dust deposition fluxes appear so stratified in the Pacific Ocean and appear so stratified in the Pacific Ocean and the Pacific Southern Ocean (SO) region compared region compared to the observational data (Fig. 3b and d) but could also indicate a model shortcoming in the representation of the dust deposition process on small scales. Finally, it should be taken into account that we compare (simulated) aeolian dust deposition fluxes onto the ocean surface to marine sediment data, i.e., any horizontal transport processes of the sediments deposited in the ocean are not also considered.

Sediment core analysis suggests that the total dust deposition flux during glacials over the Pacific SO is about 50 % of that over the Atlantic (Lamy et al., 2014), which can also be observed in our simulation results (Fig. 3d), revealing that the average dust deposition flux is around $1 \text{ g m}^{-2} \text{ yr}^{-1}$ in the Pacific SO and around $2 \text{ g m}^{-2} \text{ yr}^{-1}$ in the Atlantic Ocean. The globally averaged LGM-to-PI ratio of 5.6 found with ECHAM6.3-HAM2.3 (see Table 3) is slightly above the assumed 2- to 5-fold increase found in the literature (e.g., Kohfeld and Harrison, 2001). However, the 25-fold increase in dust deposition over Antarctica suggested by ice core data (Lambert et al., 2008) is in good accordance with our simulation results. Additionally, the observed 1- to 4-fold increase in dust depositions over the Atlantic is captured well

by the model. As a consequence of the underestimation in the PI simulation, the dust deposition ratio is systematically too high for the Tasman Sea and the Pacific Ocean (Fig. 3f). Despite this, the model yields acceptable results in terms of absolute values for LGM climate conditions.

3.2.3 Dust provenance studies

In order to identify the relative contribution of the major dust source regions southern South America, southern Africa, and Australia to the total dust deposition in the Southern Hemisphere, four additional simulations for both PI and LGM were performed. In each of them, source regions in the Southern Hemisphere were independently switched on and off, while in all experiments all dust source regions in the Northern Hemisphere are still considered. The four simulations consist of a South America-only run (SAMonly, southern Africa and Australia switched off), a southern Africa-only run (SAFonly, South America and Australia switched off), an Australia-only run (AUSonly, South America and southern Africa switched off), and a Northern Hemisphere-only run (NORTHonly, all sources in the Southern Hemisphere switched off) in order to identify the contribution of interhemispheric dust. Although New Zealand is discussed as a potential additional dust source during the LGM (Lamy et al., 2014; Koffman et al., 2021), our model only simulates dust emissions of less than 1 Gg yr^{-1} from this region, which is effectively negligible compared to the simulated emissions of 748 Tg yr^{-1} from Australia and 36 Tg yr^{-1} from Patagonia. Since our model runs at the rather coarse spatial resolution T63 (horizontal grid size of approx. $1.8° \times 1.8°$), New Zealand's geographical expanse might only be marginally captured in our model, and thus the source strength could be underestimated.

Figure 4 reveals the relative contribution of the four major source regions South America (red), southern Africa (green), Australia (blue), and the Northern Hemisphere (yellow) to the total dust deposition in the Southern Hemisphere. For both PI and LGM, the maps reveal the typical dust transport patterns in the Southern Hemisphere, which are the south-easterly trade winds for regions close to the Equator and the westerly wind belt for regions in the high latitudes. Along the Equator, dust deposition is dominated by interhemispheric
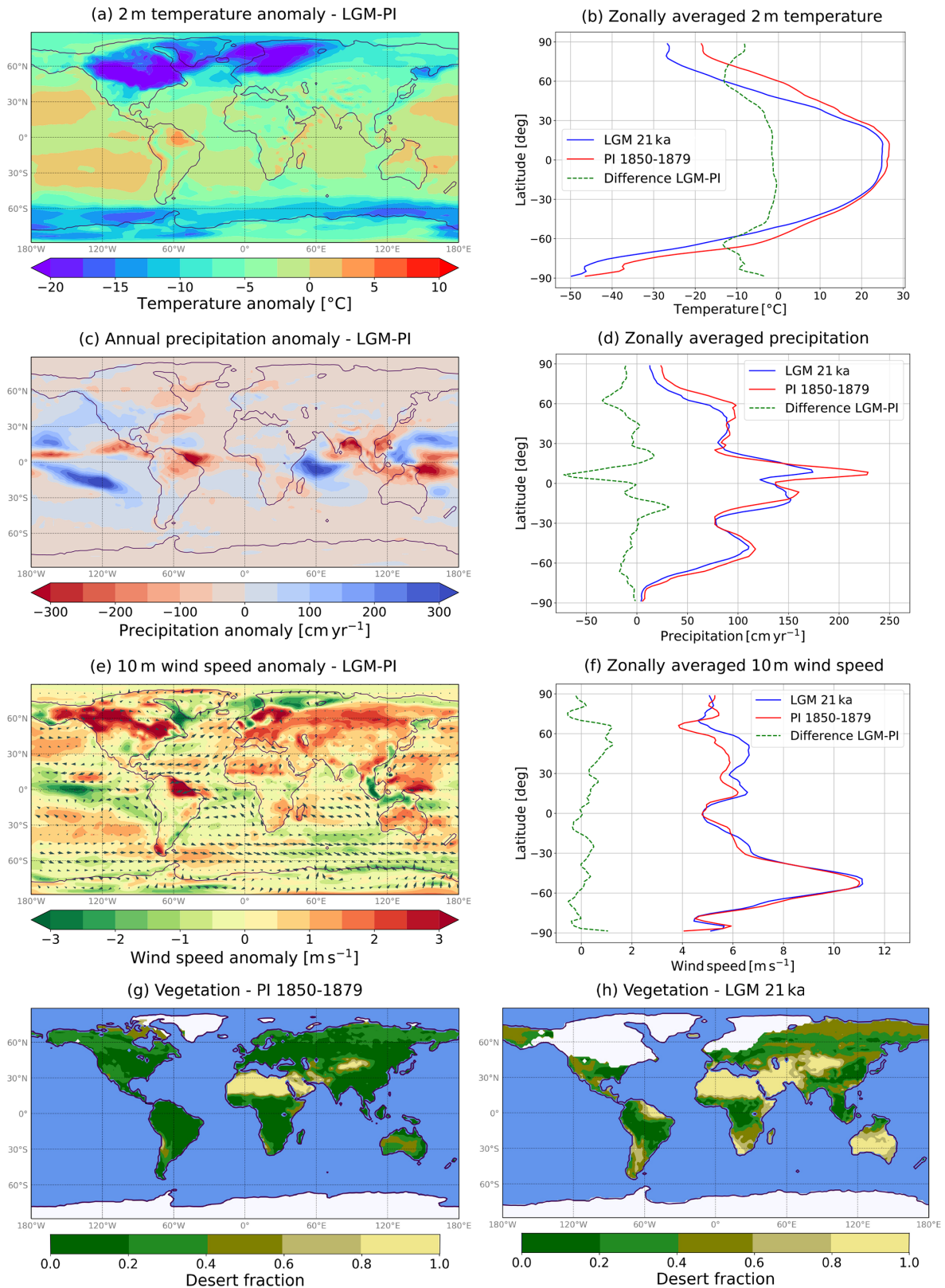
Figure 2. Global maps and zonally averaged graphs of anomalies (LGM − PI) in the 2 m temperature **(a, b)**, annual precipitation **(c, d)**, 10 m wind speed **(e, f)**, and desert fraction for each grid box for both PI and LGM **(g, h)**. Please note that glaciers (white) and the ocean (blue) have been colored in **(g)** and **(h)** for improved readability.
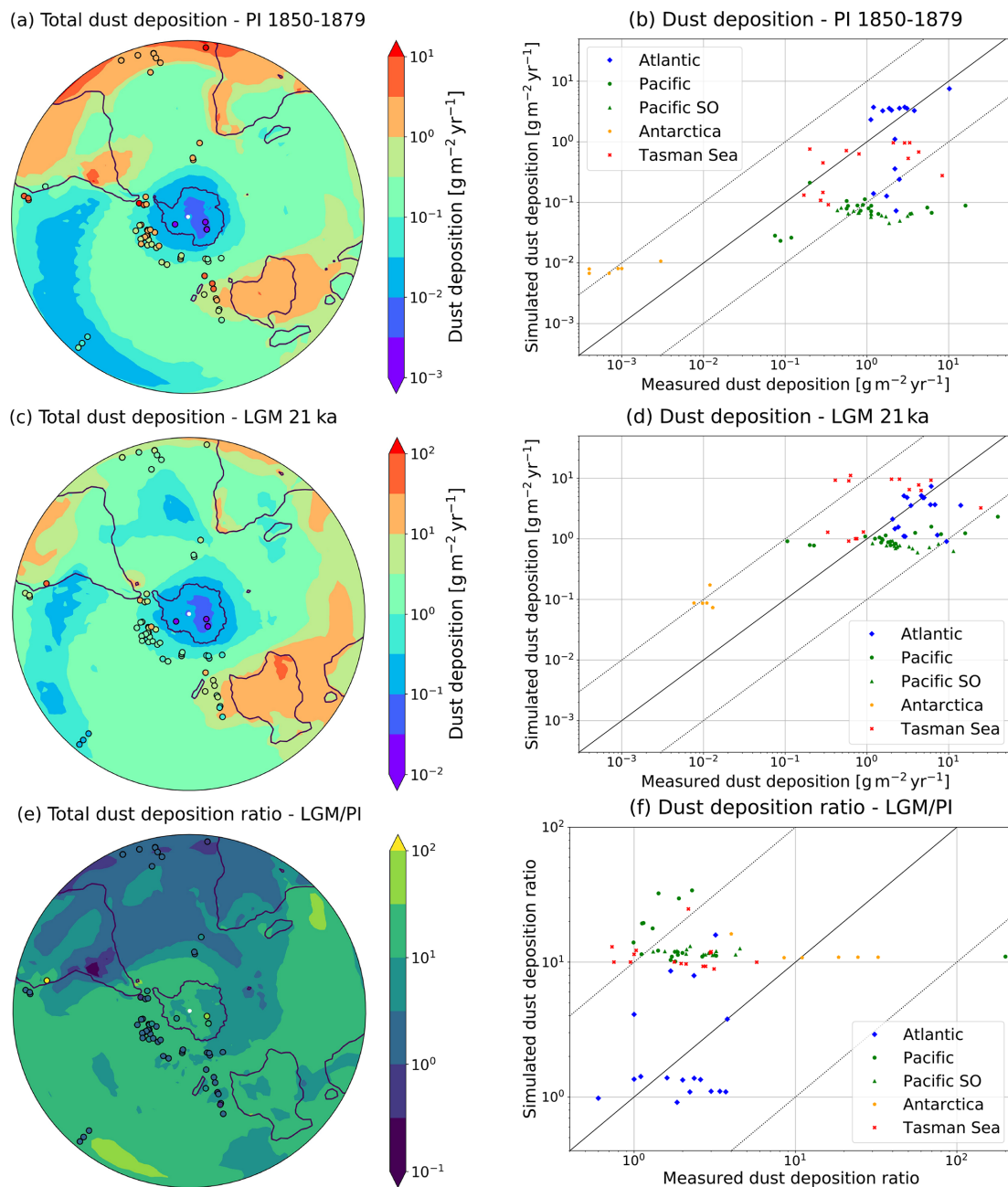
Figure 3. Comparisons between the simulated total dust deposition and observational data (Kohfeld et al., 2013) (in g m^{-2} yr^{-1}) from several regions in the Southern Hemisphere and the according scatter plots for the PI **(a, b)** and LGM **(c, d)**. Panels **(e)** and **(f)** show the according simulated and measured dust deposition ratio LGM/PI. Please note the different value ranges in **(a)** and **(c)**.

dust originating from the Northern Hemisphere. For Antarctica, our experiments reveal for PI (Fig. 4a) that the deposited dust is coming from Australia and South America, of which the latter is predominant and contributes between 60 % and 80 % of the dust deposition over West Antarctica. Despite a significant increase in dust source strength of South America (Fig. 1b, Table 3) during the LGM that is similar to Australia, its relative contribution to the total dust deposition over

the Southern Ocean and Antarctica decreases (Fig. 4b). We find that dust deposited over the SO in the eastern half of the Southern Hemisphere originates mainly from southern South America, while dust deposited over the Pacific Ocean and Pacific SO is mainly of Australian origin. Those two sources generally contribute in sum slightly more than 90 % to the total dust deposition over the SO and Antarctica (60–90° S) for both PI and LGM conditions (Table 5).

(a) Dust deposition contribution [%] - PI 1850-1879   (b) Dust deposition contribution [%] - LGM 21 ka
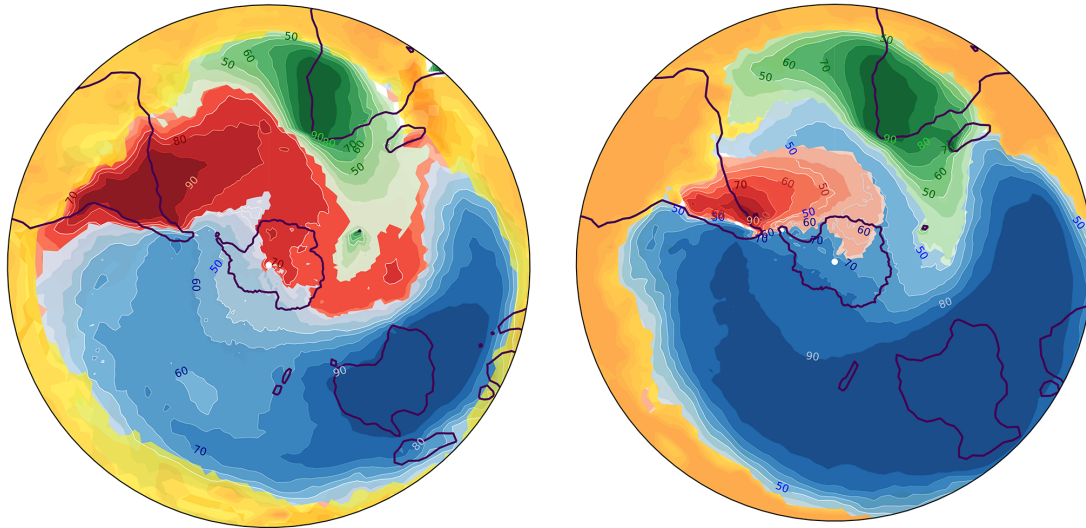
Figure 4. Results of the provenance studies showing the respective contribution of the major dust source regions South America (red), southern Africa (green), Australia (blue), and the Northern Hemisphere (yellow) to the total dust deposition in the Southern Hemisphere as a percentage (white and blue numbers; different colors were merely chosen for improved readability) for PI **(a)** and LGM **(b)**. Note that the Kerguelen Islands have been considered a dust source in the SAFonly experiment and thus appear in the same color style applied for southern Africa.

Table 5. Dust deposition onto Antarctica during the PI and LGM depending on the dust provenance (in $Tg\,yr^{-1}$ and percent).

Deposition region		All sources $[Tg\,yr^{-1}]$	Australia $[Tg\,yr^{-1}]$	South America $[Tg\,yr^{-1}]$	Southern Africa $[Tg\,yr^{-1}]$	Northern Hemisphere $[Tg\,yr^{-1}]$
Southern Ocean	PI 1850–1879	1.04	0.38 (37 %)	0.56 (54 %)	0.09 (8 %)	0.01 (1 %)
	LGM 21 ka	13.48	9.25 (69 %)	3.07 (23 %)	0.96 (7 %)	0.20 (1 %)
Antarctica	PI 1850–1879	0.21	0.06 (29 %)	0.13 (62 %)	0.02 (9 %)	0.00 (0 %)
	LGM 21 ka	2.88	1.96 (68 %)	0.69 (24 %)	0.19 (7 %)	0.03 (1 %)

Due to the interactive coupling of mineral dust in our model, we checked whether the reduced dust load in the Southern Hemisphere resulted in a shift in the zonally averaged precipitation and found no shifts regardless of the switched-off sources. The procedure and the findings are in agreement with results by Evans et al. (2020), who performed similar experiments in order to investigate the influence of the dust load asymmetry between the Northern Hemisphere and Southern Hemisphere on the location of the Intertropical Convergence Zone (ITCZ) as a consequence of the resulting asymmetric radiative forcing. They likewise found that the influence of the Southern Hemisphere is almost negligible compared to the Northern Hemisphere due to the much smaller contribution to the total global atmospheric dust load. Those findings raise the confidence that our experiments yield meaningful results. Our model results for PI agree well with those found by Li et al. (2008) for current climate conditions using the GFDL Atmospheric General Circulation Model AM2, particularly the dominance of south-

ern South American dust deposited over West Antarctica and the equal contributions of Australian and South American dust deposited over East Antarctica. The discussed combined contribution of Australia and South America of more than 90 % to the total dust deposition over the Southern Ocean and Antarctica is again in accordance with results by Li et al. (2008), who found a combined contribution of more than 85 %. However, our identification of Australia as the predominant source for dust deposited over Antarctica during the LGM is inconsistent with observational data from Antarctic ice cores. The characteristic ratios of Sr and Nd isotopes suggest southern South America to be the most likely dust source, possibly with minor contributions up to 15 % from Australian or southern African dust sources (Basile et al., 1997; Delmonte et al., 2008). Our contradicting results clearly indicate a shortcoming on the modeling side, and our further analysis is intended to uncover the mechanism causing this discrepancy.

Although both Australian and South American dust sources increase by a factor of around 15 in our model during the LGM compared to the PI (Table 3), the absolute amount of dust coming from Australia clearly dominates the Southern Hemisphere. Only in a smaller region of East Antarctica does dust of South American origin contribute up to 40 % of the total deposition. The deposition pattern of Australian dust shown in Fig. 4b suggests an increased long-range transport, which can likely be attributed to the higher particle lifetime during the LGM as a consequence of the generally drier climate in the Southern Hemisphere (Fig. 2c and d). At first glance, it seems that this should apply to dust coming from both Australian and southern South American sources and might consequently not provide a possible explanation for the decrease in the relative contribution of southern South American dust to the total deposition. However, as discussed in Sect. 3.2.1, we found that the regional climate over Patagonia and parts of the Atlantic area of the Southern Ocean turned out to be slightly wetter during the LGM (Fig. 2c). Since the westerly wind belt is responsible for the dust transport at these latitudes, this suggests that dust of South American origin was removed by scavenging with a higher efficiency, while dust coming from Australia might have had higher particle lifetimes due to the drier climate simulated over the Pacific Ocean and Pacific SO.

3.2.4 Particle lifetime and radius anomalies in the Southern Hemisphere during the LGM

In order to test this hypothesis of changed glacial particle lifetimes, we investigate the particle lifetime anomaly (Fig. 5a). The correlation between the particle lifetime anomaly and the precipitation anomaly (Fig. 5b) can easily be recognized, which is not surprising considering the fact that in Sect. 3.1 wet scavenging was identified as the predominant deposition mechanism in our model. Especially in regions close to the Equator, for instance in the Pacific Ocean and the Indian Ocean but also more southwards in the Atlantic Ocean and Southern Ocean around 60° S, the pattern of increased precipitation causing shorter particle lifetimes can be clearly seen. To get more insights into the decrease of the relative importance of southern South American dust concerning the total dust deposition onto the Southern Ocean and Antarctica, the particle lifetime southwards of the horse latitudes (30° S) were analyzed, since dust closer to the Equator is essentially transported northeastwards by the trade winds. On average, the drier climate south of 30° S during the LGM leads to an increased particle lifetime of +0.52 d. However, using the results of our provenance studies, we find that the average particle lifetime of Australian dust increases by +1.12 d, whereas it decreases by −1.69 d for dust particles of southern South American origin. Since the particle lifetime eventually influences the transport range, the over-proportional importance of Australian dust in the Southern Hemisphere during the LGM compared to PI conditions (Fig. 4a and b), particularly south of 60° S, can thus be explained by changes in the regional precipitation patterns.

Combining our results concerning changes in particle lifetime with our provenance studies, we want to take up on the ongoing debate whether changes in source strength or atmospheric particle lifetime were mainly responsible for the increased dust concentration during the LGM found in Antarctic ice cores. Figure 5c and d and Table 6 clearly show that wet scavenging is the main deposition mechanism for mineral dust between 60 and 90° S in our model, particularly over the Southern Ocean, which is in agreement with the study of Markle et al. (2018), who found that precipitation is the "principal barrier to aerosols reaching the poles". However, while the authors suggest that changes in particle lifetime are the main reason for the increased dust transport to Antarctica during glacials, the generally drier climate during the LGM simulated by our model only leads to a slightly higher particle lifetime on average. Of bigger importance in the scope of our simulations are the regional changes in precipitation, and thus in particle lifetime, because they eventually lead to Australia becoming the predominant source of dust deposited over Antarctica. Although our model overestimates the dust deposition over Antarctica for both PI and LGM by an order of magnitude (Fig. 3b and d), the simulated LGM-to-PI ratio of 14 (Table 5) is generally in good agreement with observations (Fig. 3e and f). Apparently, the almost 16-fold increase in dust source strength during the LGM compared to PI for both southern South America and Australia (Table 3) is necessary to achieve this accordance. Furthermore, the simulated increase in source activity during the LGM can be traced back to increases in wind speed over the source areas, reduced vegetation, a generally drier climate, and extended source regions due to a lower sea level. In particular, in southern South America extended source regions contribute more than 80 % to the dust emissions during the LGM (Table 4). Our findings are in agreement with results by Wolff et al. (2010), who suggested that the variability in the non-sea-salt calcium flux (as an elemental marker for terrestrial dust most likely originating from South America) on glacial–interglacial timescales found in Antarctic ice cores was caused by changes in the source region rather than by changes in atmospheric particle lifetime.

Finally, we have a look at particle size anomalies between the LGM and the PI in the Southern Hemisphere. Here, the focus is only on the insoluble modes, since the model assumes perfectly internally mixed soluble modes, and thus the according particles do not consist of only mineral dust. The simulations show a clear trend of increasingly coarser particles for both the accumulation and the coarse mode in the Southern Hemisphere between the source areas and the South Pole (Fig. 5e and f). Additionally, our results suggest a correlation between coarser particles and increased particle lifetimes and reduced precipitation (Fig. 5a and b).

The observed size variability between cold and warm climate states has been used to draw conclusions about me-
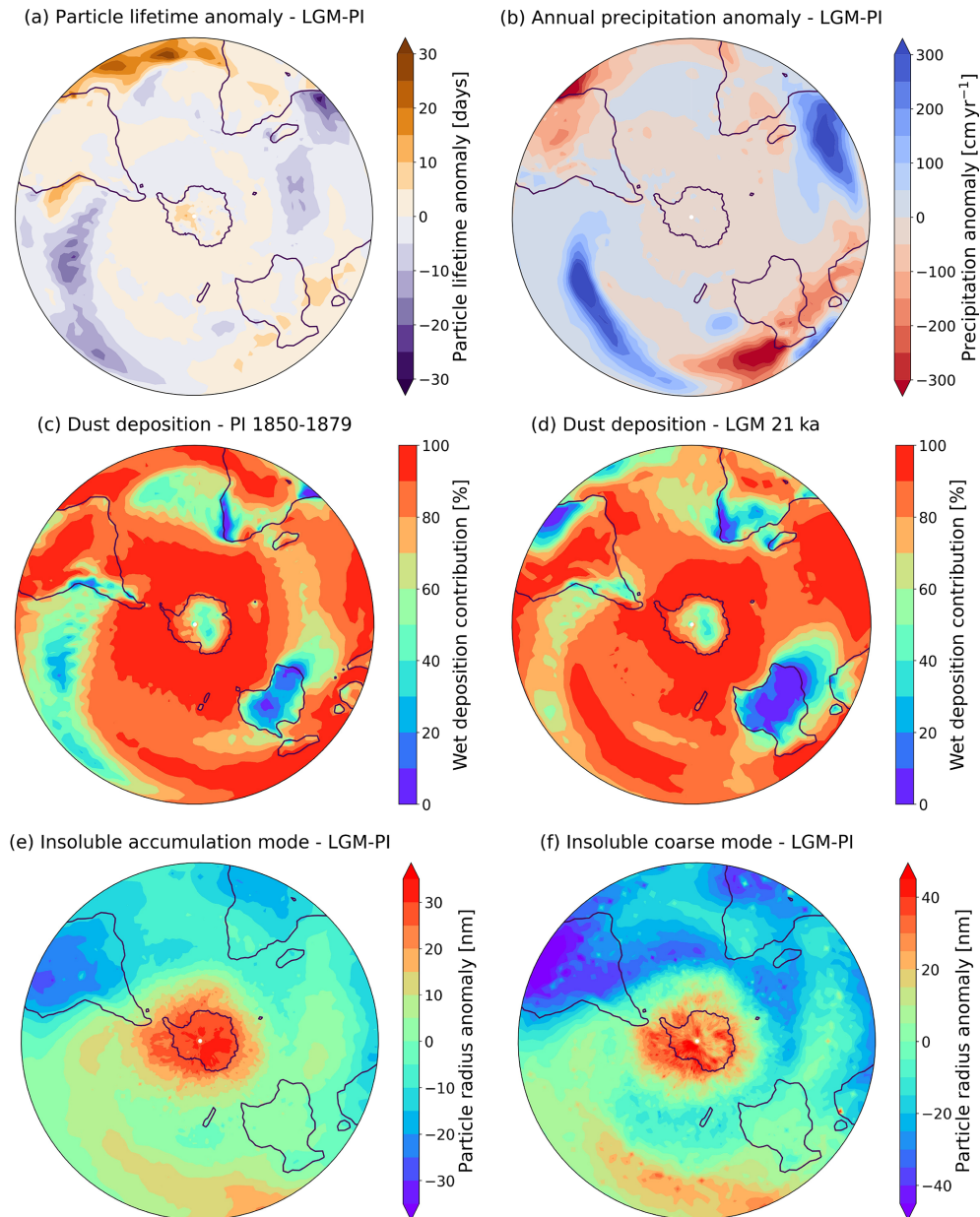
Figure 5. Particle lifetime anomalies (LGM-PI) (in d) **(a)**, annual precipitation anomalies (in cm yr^{-1}) **(b)**, and the contribution of wet deposition to the total deposition (in percent) for both the PI **(c)** and LGM **(d)** in the Southern Hemisphere. Additionally, particle radius anomalies (in nm) are shown for the insoluble accumulation **(e)** and insoluble coarse mode **(f)**.

Table 6. Contribution of dust deposition mechanisms to the total dust deposition between 30 and 90° S during the PI and LGM in percent.

Deposition region		Wet deposition [%]	Dry deposition [%]	Sedimentation [%]
30–60° S	PI 1850–1879	79	8	13
	LGM 21 ka	68	13	19
60–90° S	PI 1850–1879	91	1	8
	LGM 21 ka	92	0	8

teorological conditions. On the one hand, the analysis of mineral dust retrieved from marine sediments (Hovan et al., 1991) and Greenland ice cores (Steffensen, 1997) consistently showed the deposition of coarser dust particles during glacials, which has been interpreted as either being consequence of stronger winds or the result of decreased weathering (Mahowald et al., 2014). On the other hand, dust retrieved from Antarctic ice cores shows spatially varying and opposing trends with respect to particle sizes during cold climates. For instance, a particle size analysis of mineral dust retrieved from the EPICA-Dome C (EDC) ice core (75°06′ S, 123°21′ E) indicates the deposition of finer particles during the LGM compared to deposition occurring during the warmer climate of the Holocene (10 ka), while the same analysis for an ice core drilled at the Dome B (DB) location (77°05′ S, 106°48′ E) yields the deposition of coarser particles during the LGM compared to the Holocene (Delmonte et al., 2004). Since the mineralogical analysis of the dust particles clearly shows that the isotopic ratios match southern South American sources for both locations, it can be concluded that the deposited dust was of the same geographical provenance. Consequently, the observed differences are assumed to be caused by changes in the atmospheric circulation. As coarser particles tendentially have a shorter particle lifetime, those found at DB during the LGM are likely the result of shorter trajectories, while the finer particles and the increased sorting of the particles, expressed by a comparably small σ found for the LGM (Delmonte et al., 2002), indicate longer pathways from the source to the deposition area. The relative increase of finer particles in the EDC region during the LGM has also been confirmed by modeling studies (e.g., Mahowald et al., 2006). The model used by Albani et al. (2012) also showed the deposition of slightly coarser particles in regions of East Antarctica and a shift to generally finer particles in most other regions of Antarctica during the LGM, as indicated by ice core data (Delmonte et al., 2002, 2004). The authors explain the regional variation in particle size, on the one hand, by reduced wet deposition during transport, which leads to the general shift to finer particles, and suggest, on the other hand, that size-selective dry deposition dominates in the interior of Antarctica, which in turn leads to the regional deposition of slightly coarser particles. Our model results support the suggested spatial variation in the respective predominant deposition mechanisms (Fig. 5e and f). Similar opposing dust grain size trends over glacial–interglacial timescales have also been found in marine sediments retrieved from the South Pacific and South Atlantic (van der Does et al., 2021).

Our findings of generally coarser particles for both the accumulation and the coarse mode in the Southern Hemisphere between the source areas and the South Pole without any remarkable regional differences contradict the previous discussion. For technical reasons, the mass median radius and the standard deviation of the particle size distribution in the scope of the dust emission process are both fixed parameters

in our model for both the insoluble accumulation and the insoluble coarse mode (see Sect. 3.2.1 and Stier et al., 2005). Consequently, the emission of coarser particles during the LGM due to stronger winds in the source regions must be excluded. Since the standard deviation of the particle size distributions are kept constant for all modes, HAM2.3 also does not account for features like a more efficient particle sorting due to longer particle lifetimes as discussed above. The only mechanism in the model leading to increased particle sizes is the coagulation of insoluble dust particles with sulfuric acid particles of much smaller size (Vignati et al., 2004). Consequently, the observed particle size anomalies in the Southern Hemisphere during the LGM compared to the PI shown in Fig. 5e and f can be attributed to an increased sulfur coating of the insoluble dust particles as a consequence of the longer particle lifetimes (Fig. 5a) due to reduced precipitation (Fig. 5b). These findings were tested by running the same simulation while switching off all sulfate sources, and the observed particle radius anomalies did indeed vanish.

3.2.5 Meridional dust transport in the Southern Hemisphere during PI and LGM

Although the particle size distribution implemented in HAM2.3 does not allow for the investigation of size-dependent processes within a given mode during transport, general transport patterns on larger scales can still be studied. Here, the meridional transport from the source areas in the Southern Hemisphere towards the South Pole is of particular interest. As a consequence of the Coriolis force, southward-moving air parcels carrying mineral dust are generally deviated eastwards, leading predominantly to a zonal transport and distribution of dust by the westerlies, whereas the meridional transport is caused by eddies (Li et al., 2010). Figure 6 shows the zonally averaged dust mass concentration depending on the altitude south of 30° S for both the PI (Fig. 6a and b) and the LGM (Fig. 6c and d), as well as the mean dust transport height for all modes and times (Fig. 6e). The general meridional dust transport pathway can be understood as a result of prevailing convective cells. After their emission in the mid-latitudes and low latitudes, dust particles are transported to the mid-troposphere and high troposphere (and potentially even higher to the tropopause; see below) along the polar front, i.e., the boundary between the Ferrel and the polar cell, by convection. While removal processes like sedimentation and dry deposition take place close to the ground, dust particles transported in the troposphere are mostly removed by wet scavenging. Dust particles transported at higher altitudes, however, remain significantly longer in the atmosphere and can only get removed once they reach lower altitudes as a consequence of the convergence and subsequent sinking of cold air masses (so-called subsidence) close to the South Pole (James, 1989). As can be clearly recognized in Fig. 6 for both the PI and the LGM, the finer particles of the accumulation mode are transported

at higher altitudes compared to particles in the coarse mode. This effect is caused by the higher sedimentation velocities of larger particles and has also been found in other studies (Tegen and Fung, 1994). Delmonte et al. (2004) used this insight in order to explain the differences in dust grain size at DB and EDC during the LGM (see above) despite their geographical proximity and same dust provenance. The authors suggest that the measured difference in particle size and grading (i.e., low σ) are caused by finer particles being transported on longer trajectories in the upper atmosphere and deposited in regions of air subsidence, whereas coarse particles were transported to the respective deposition areas by comparably short trajectories in the troposphere. This opposing temporal trend with respect to the measured particle size of dust deposited at DB and EDC during the LGM–Holocene transition is proposed to be the result of vortex migration, i.e., the southwards movement of an area of preferential upper-air subsidence on the corresponding timescale (Delmonte et al., 2004).

While differences in transport height between particles of the accumulation and the coarse mode can be observed for a given time period, obvious differences also exist with respect to transport height between the PI and the LGM for a given mode. During the PI, the majority of dust particles in the accumulation (Fig. 6a) and the coarse mode (Fig. 6b) seem to get transported quickly by convection from the source regions to a typical altitude of 11 and 9 km, respectively, at around 50° S and then follow a rather meridional pathway southward mostly at the same altitude. The southwards-directed meridional transport of mineral dust during the LGM, however, does not exhibit such clear vertical and horizontal patterns. Instead, the altitude seems to increase continuously during the southward transport, reaching a maximum of around 8 and 6 km for the accumulation (Fig. 6c) and the coarse mode (Fig. 6d), respectively. The obtained difference in mean transport height (Fig. 6e) between the PI and the LGM can be attributed to reduced vertical mixing and advection as a consequence of colder surfaces (Fig. 2a and b), leading to a higher dust concentration at lower levels (Albani et al., 2012). These results suggest that the polar cell was vertically less extended during the LGM compared to the warmer PI climate.

4   Conclusions

ECHAM6.3-HAM2.3 constitutes a state-of-the-art model providing an interactive coupling of mineral dust emissions to the atmospheric model depending on surface properties and meteorological factors. For present-day conditions, the model yields reasonable results for dust emission, burden, and deposition close to the median of other studies performed in the scope of the global dust model intercomparison in AeroCom phase I. Generally, our model performs at the lower end of the 1000 to 4000 Tg yr^{-1} range of dust emissions es-

timated by the IPCC, which is caused by the neglect of a super-coarse particle mode. The predominant representation of fine and coarse particles leads to slightly higher particle lifetimes, which in turn enables the long-range transport of mineral dust to remote regions and causes wet scavenging to become the most dominant deposition mechanism in our model.

For pre-industrial climate conditions, a comparison to other modeling studies and measurement data suggests that in absolute numbers, the simulated dust emissions and depositions are too low, particularly in the Southern Hemisphere. The discrepancy is greatest in the South Pacific, suggesting that the dust source strength of Australia is underestimated in the model. However, since the simulated dust deposition in the Tasman Sea and over Antarctica are in good agreement with and slightly higher than the observational data, respectively, this model–data mismatch cannot be easily explained by a sole model source strength deficit, and non-aeolian contributions not considered in our model might play a crucial role. For LGM climate conditions, the simulated dust deposition fluxes agree well with measurement data. As a consequence of the underestimation of the dust cycle during PI, the corresponding simulated globally averaged LGM to PI ratio with respect to dust depositions of 5.6 is slightly above the 2 to 5 suggested based on measurement data. A regional analysis in the Southern Hemisphere shows that the increase in dust emissions of the major sources of southern South America, southern Africa, and Australia during the LGM can be attributed to a generally drier climate causing less precipitation (except over Patagonia), extended source regions due to a lower sea level, and significantly stronger winds in the source regions combined with reduced vegetation.

Our dust provenance studies indicate that over 90 % of the dust deposited between 30 and 90° S is either of Australian or South American origin for both the PI and LGM climate conditions. However, our model suggests that Australia constituted the predominant source of dust deposited over Antarctica during the LGM. This result is inconsistent with several data studies suggesting based on isotope analysis that most of the dust deposited over Antarctica during the LGM is most likely of southern South American origin and clearly indicates a shortcoming on the modeling side. Although both the South American and Australian sources show an almost equal increase in strength during the LGM compared to the PI in our model, the relative contribution of South America decreases. This can be traced back to an average increase in particle lifetime of Australian dust during the LGM, whereas the average particle lifetime of South American dust decreases due to changes in regional precipitation pattern. Despite a slight increase in particle lifetime in the Southern Hemisphere during the LGM due to the generally drier climate, the almost 16-fold source strength increase of the contributions of southern South America and Australia during the LGM compared to the PI seems to be necessary in order to achieve a on average 14-fold increase in dust de-
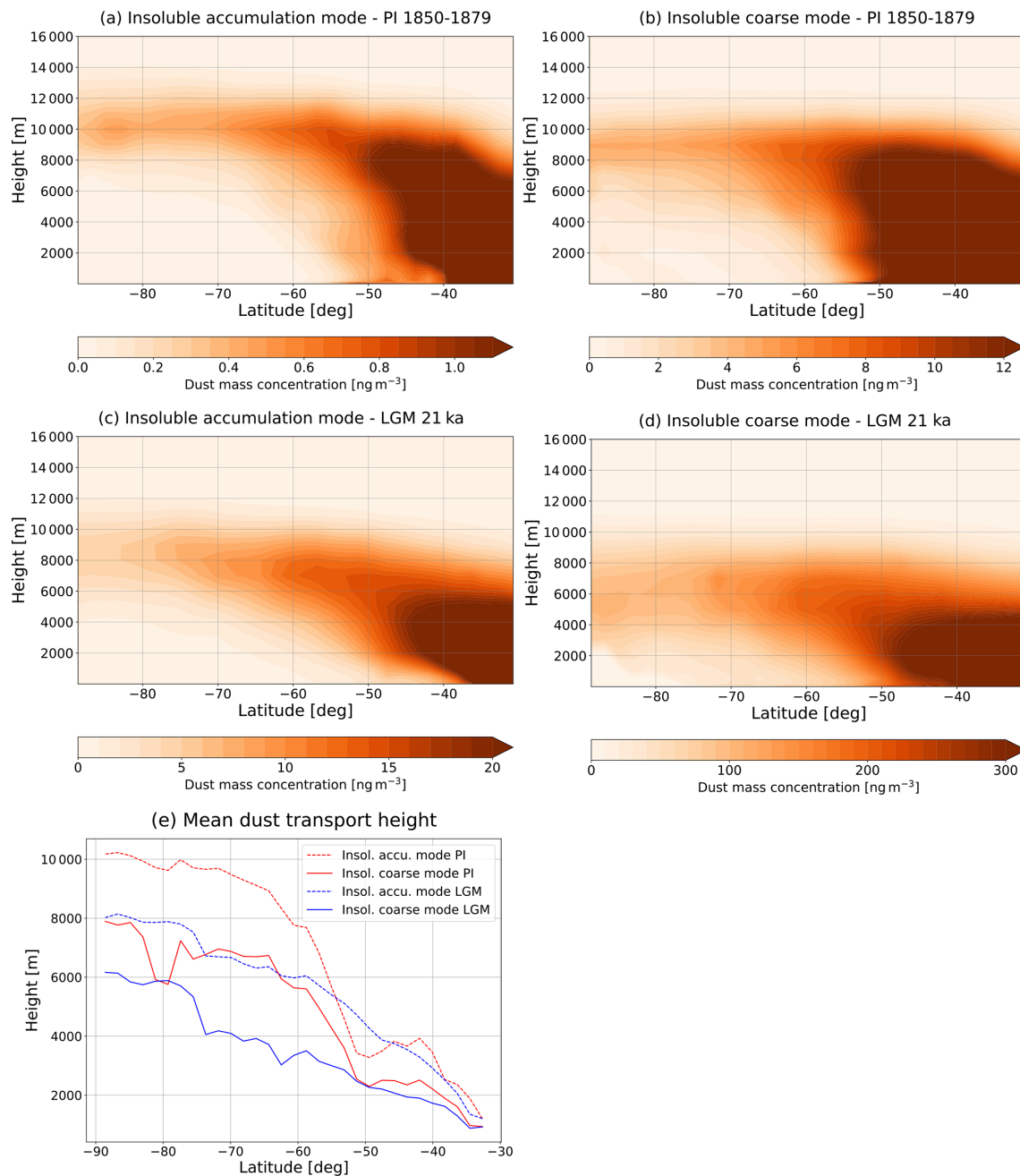
Figure 6. Zonally averaged dust concentration depending on the altitude for the insoluble accumulation and coarse mode between 30 and 90° S during the PI (**a, b**) and LGM (**c, d**). The mean transport height for all modes and simulation periods (**e**).

position over Antarctica in our simulations, which is in good accordance with observational data.

For both the PI and LGM, the finer particles in the accumulation mode are transported at greater altitudes than coarse mode particles within the Southern Hemispheric troposphere due to lower sedimentation velocities. Additionally, both modes exhibit a clear trend of being transported at lower altitudes during the LGM, which can be explained by re-

duced convection due to colder surfaces and indicate that the Polar cell was vertically less extended during the LGM.

Our study clearly showed the capabilities and limitations of ECHAM6.3-HAM2.3. Specifically, microphysical effects can only be studied to some degree since all particles within a given mode are assumed to have the same physical and chemical properties. Since SSTs influence precipitation patterns and other climate elements like wind speed, which in turn affect the dust emission process, prescribing different bound-

ary conditions based on reconstructions suggesting cooler SSTs might turn out to be a useful approach to reduce the data–model discrepancy, particularly in regard to the provenance of dust deposited over Antarctica during the LGM. Future sensitivity studies might yield new insights into this matter.

References

Abdul-Razzak, H. and Ghan, S.: A parameterization of aerosol activation: 2. Multiple aerosol types, J. Geophys. Res., 105, 6837–6844, https://doi.org/10.1029/1999JD901161, 2000.

Albani, S. and Mahowald, N. M.: Paleodust Insights into Dust Impacts on Climate, J. Climate, 32, 7897–7913, https://doi.org/10.1175/JCLI-D-18-0742.1, 2019.

Albani, S., Mahowald, N. M., Delmonte, B., Maggi, V., and Winckler, G.: Comparing modeled and observed changes in mineral dust transport and deposition to Antarctica between the Last Glacial Maximum and current climates, Clim. Dynam., 38, 1731–1755, https://doi.org/10.1007/s00382-011-1139-5, 2012.

Albani, S., Mahowald, N. M., Perry, A. T., Scanza, R. A., Zender, C. S., Heavens, N. G., Maggi, V., Kok, J. F., and Otto-Bliesner, B. L.: Improved dust representation in the Community Atmosphere Model, J. Adv. Model. Earth Sy., 6, 541–570, https://doi.org/10.1002/2013MS000279, 2014.

Albani, S., Mahowald, N. M., Murphy, L. N., Raiswell, R., Moore, J. K., Anderson, R. F., McGee, D., Bradtmiller, L. I., Delmonte, B., Hesse, P. P., and Mayewski, P. A.: Paleodust variability since the Last Glacial Maximum and implications for iron inputs to the ocean, Geophys. Res. Lett., 43, 3944–3954, https://doi.org/10.1002/2016GL067911, 2016.

Balkanski, Y., Schulz, M., Claquin, T., and Guibert, S.: Reevaluation of Mineral aerosol radiative forcings suggests a better agreement with satellite and AERONET data, Atmos. Chem. Phys., 7, 81–95, https://doi.org/10.5194/acp-7-81-2007, 2007.

Basile, I., Grousset, F. E., Revel, M., Petit, J. R., Biscaye, P. E., and Barkov, N. I.: Patagonian origin of glacial dust deposited in East Antarctica (Vostok and Dome C) during glacial stages 2, 4 and 6, Earth Planet. Sci. Lett., 146, 573–589, https://doi.org/10.1016/S0012-821X(96)00255-5, 1997.

Boucher, O.: Atmospheric Aerosols: Properties and Climate Impacts, Springer, Netherlands, https://doi.org/10.1007/978-94-017-9649-1, 2015.

Brinkop, S. and Roeckner, E.: Sensitivity of a general circulation model to parameterizations of cloud–turbulence interactions in the atmospheric boundary layer, Tellus A, 47, 197–220, https://doi.org/10.1034/j.1600-0870.1995.t01-1-00004.x, 1995.

Cheng, T., Peng, Y., Feichter, J., and Tegen, I.: An improvement on the dust emission scheme in the global aerosol-climate model ECHAM5-HAM, Atmos. Chem. Phys., 8, 1105–1117, https://doi.org/10.5194/acp-8-1105-2008, 2008.

Clark, P. U., Dyke, A. S., Shakun, J. D., Carlson, A. E., Clark, J., Wohlfarth, B., Mitrovica, J. X., Hostetler, S. W., and McCabe, A. M.: The Last Glacial Maximum, Science, 325, 710–714, https://doi.org/10.1126/science.1172873, 2009.

Croft, B., Lohmann, U., Martin, R. V., Stier, P., Wurzler, S., Feichter, J., Posselt, R., and Ferrachat, S.: Aerosol size-

dependent below-cloud scavenging by rain and snow in the ECHAM5-HAM, Atmos. Chem. Phys., 9, 4653–4675, https://doi.org/10.5194/acp-9-4653-2009, 2009.

Croft, B., Lohmann, U., Martin, R. V., Stier, P., Wurzler, S., Feichter, J., Hoose, C., Heikkilä, U., van Donkelaar, A., and Ferrachat, S.: Influences of in-cloud aerosol scavenging parameterizations on aerosol concentrations and wet deposition in ECHAM5-HAM, Atmos. Chem. Phys., 10, 1511–1543, https://doi.org/10.5194/acp-10-1511-2010, 2010.

De Deckker, P., Norman, M., Goodwin, I. D., Wain, A., and Gingele, F. X.: Lead isotopic evidence for an Australian source of aeolian dust to Antarctica at times over the last 170,000 years, Palaeogeogr. Palaeocl., 285, 205–223, https://doi.org/10.1016/j.palaeo.2009.11.013, 2010.

Delmonte, B., Petit, J., and Maggi, V.: Glacial to Holocene implications of the new 27000-year dust record from the EPICA Dome C (East Antarctica) ice core, Clim. Dynam., 18, 647–660, https://doi.org/10.1007/s00382-001-0193-9, 2002.

Delmonte, B., Petit, J.-R., Andersen, K., Basile-Doelsch, I., Maggi, V., and Lipenkov, V.: Dust size evidence for opposite regional atmospheric circulation changes over East Antarctica during the last climatic transition, Clim. Dynam., 23, 427–438, https://doi.org/10.1007/s00382-004-0450-9, 2004.

Delmonte, B., Andersson, P. S., Hansson, M., Schöberg, H., Petit, J. R., Basile-Doelsch, I., and Maggi, V.: Aeolian dust in East Antarctica (EPICA-Dome C and Vostok): Provenance during glacial ages over the last 800 kyr, Geophys. Res. Lett., 35, L07703, https://doi.org/10.1029/2008GL033382, 2008.

Dufresne, J.-L., Gautier, C., Ricchiazzi, P., and Fouquart, Y.: Longwave Scattering Effects of Mineral Aerosols, J. Atmos. Sci., 59, 1959–1966, https://doi.org/10.1175/1520-0469(2002)059<1959:LSEOMA>2.0.CO;2, 2002.

Durack, P. J. and Taylor, K. E.: input4MIPs.CMIP6.CMIP.PCMDI.PCMDI-AMIP-1-1-6, Earth System Grid Federation, https://doi.org/10.22033/ESGF/input4MIPs.12381, 2019.

Evans, S., Dawson, E., and Ginoux, P.: Linear Relation Between Shifting ITCZ and Dust Hemispheric Asymmetry, Geophys. Res. Lett., 47, e2020GL090499, https://doi.org/10.1029/2020GL090499, 2020.

Goudie, A. S.: The History and Nature of Wind Erosion in Deserts, Annu. Rev. Earth Pl. Sc., 36, 97–119, https://doi.org/10.1146/annurev.earth.36.031207.124353, 2008.

Hagemann, S. and Stacke, T.: Impact of the soil hydrology scheme on simulated soil moisture memory, Clim. Dynam., 44, 1731–1750, https://doi.org/10.1007/s00382-014-2221-6, 2015.

HAMMOZ consortium: ECHAM6-HAMMOZ model data, available at: https://redmine.hammoz.ethz.ch/projects/hammoz/repository/1/show/echam6-hammoz/branches/tanja, last access: 14 September 2020.

Hovan, S. A., Rea, D. K., and Pisias, N. G.: Late Pleistocene Continental Climate and Oceanic Variability Recorded in Northwest Pacific Sediments, Paleoceanography, 6, 349–370, https://doi.org/10.1029/91PA00559, 1991.

Huneeus, N., Schulz, M., Balkanski, Y., Griesfeller, J., Prospero, J., Kinne, S., Bauer, S., Boucher, O., Chin, M., Dentener, F., Diehl, T., Easter, R., Fillmore, D., Ghan, S., Ginoux, P., Grini, A., Horowitz, L., Koch, D., Krol, M. C., Landing, W., Liu, X., Mahowald, N., Miller, R., Morcrette, J.-J., Myhre, G., Pen-

ner, J., Perlwitz, J., Stier, P., Takemura, T., and Zender, C. S.: Global dust model intercomparison in AeroCom phase I, Atmos. Chem. Phys., 11, 7781–7816, https://doi.org/10.5194/acp-11-7781-2011, 2011.

Intergovernmental Panel on Climate Change (Ed.): Clouds and Aerosols, in: Climate Change 2013 – The Physical Science Basis: Working Group I Contribution to the Fifth Assessment Report of the Intergovernmental Panel on Climate Change, Cambridge University Press, Cambridge, 571–658, https://doi.org/10.1017/CBO9781107415324.016, 2014.

James, I. N.: The Antarctic drainage flow: implications for hemispheric flow on the Southern Hemisphere, Antarct. Sci., 1, 279–290, https://doi.org/10.1017/S0954102089000404, 1989.

Kageyama, M., Albani, S., Braconnot, P., Harrison, S. P., Hopcroft, P. O., Ivanovic, R. F., Lambert, F., Marti, O., Peltier, W. R., Peterschmitt, J.-Y., Roche, D. M., Tarasov, L., Zhang, X., Brady, E. C., Haywood, A. M., LeGrande, A. N., Lunt, D. J., Mahowald, N. M., Mikolajewicz, U., Nisancioglu, K. H., Otto-Bliesner, B. L., Renssen, H., Tomas, R. A., Zhang, Q., Abe-Ouchi, A., Bartlein, P. J., Cao, J., Li, Q., Lohmann, G., Ohgaito, R., Shi, X., Volodin, E., Yoshida, K., Zhang, X., and Zheng, W.: The PMIP4 contribution to CMIP6 – Part 4: Scientific objectives and experimental design of the PMIP4-CMIP6 Last Glacial Maximum experiments and PMIP4 sensitivity experiments, Geosci. Model Dev., 10, 4035–4055, https://doi.org/10.5194/gmd-10-4035-2017, 2017.

Koffman, B. G., Goldstein, S. L., Winckler, G., Borunda, A., Kaplan, M. R., Bolge, L., Cai, Y., Recasens, C., Koffman, T. N. B., and Vallelonga, P.: New Zealand as a source of mineral dust to the atmosphere and ocean, Quaternary Sci. Rev., 251, 106659, https://doi.org/10.1016/j.quascirev.2020.106659, 2021.

Kohfeld, K. E. and Harrison, S. P.: DIRTMAP: the geological record of dust, Earth-Sci. Rev., 54, 81–114, https://doi.org/10.1016/S0012-8252(01)00042-3, 2001.

Kohfeld, K. E. and Ridgwell, A.: Glacial-interglacial variability in atmospheric CO_2, in: Geophysical Monograph Series, vol. 187, edited by: Le Quéré, C. and Saltzman, E. S., American Geophysical Union, Washington, D.C., 251–286, https://doi.org/10.1029/2008GM000845, 2009.

Kohfeld, K. E., Graham, R. M., de Boer, A. M., Sime, L. C., Wolff, E. W., Le Quéré, C., and Bopp, L.: Southern Hemisphere westerly wind changes during the Last Glacial Maximum: paleo-data synthesis, Quaternary Sci. Rev., 68, 76–95, https://doi.org/10.1016/j.quascirev.2013.01.017, 2013.

Lamarque, J.-F., Bond, T. C., Eyring, V., Granier, C., Heil, A., Klimont, Z., Lee, D., Liousse, C., Mieville, A., Owen, B., Schultz, M. G., Shindell, D., Smith, S. J., Stehfest, E., Van Aardenne, J., Cooper, O. R., Kainuma, M., Mahowald, N., McConnell, J. R., Naik, V., Riahi, K., and van Vuuren, D. P.: Historical (1850–2000) gridded anthropogenic and biomass burning emissions of reactive gases and aerosols: methodology and application, Atmos. Chem. Phys., 10, 7017–7039, https://doi.org/10.5194/acp-10-7017-2010, 2010.

Lambert, F., Delmonte, B., Petit, J. R., Bigler, M., Kaufmann, P. R., Hutterli, M. A., Stocker, T. F., Ruth, U., Steffensen, J. P., and Maggi, V.: Dust-climate couplings over the past 800,000 years from the EPICA Dome C ice core, Nature, 452, 616–619, https://doi.org/10.1038/nature06763, 2008.

Lamy, F., Gersonde, R., Winckler, G., Esper, O., Jaeschke, A., Kuhn, G., Ullermann, J., Martinez-Garcia, A., Lambert, F., and

Kilian, R.: Increased Dust Deposition in the Pacific Southern Ocean During Glacial Periods, Science, 343, 403–407, https://doi.org/10.1126/science.1245424, 2014.

Li, F., Ginoux, P., and Ramaswamy, V.: Distribution, transport, and deposition of mineral dust in the Southern Ocean and Antarctica: Contribution of major sources, J. Geophys. Res., 113, D10207, https://doi.org/10.1029/2007JD009190, 2008.

Li, F., Ginoux, P., and Ramaswamy, V.: Transport of Patagonian dust to Antarctica, J. Geophys. Res.-Atmos., 115, D18217, https://doi.org/10.1029/2009JD012356, 2010.

Lin, S.-J. and Rood, R.: Multidimensional Flux-Form Semi-Lagrangian Transport Schemes, Mon. Weather Rev., 124, 2046–2070, https://doi.org/10.1175/1520-0493(1996)124<2046:MFFSLT>2.0.CO;2, 1996.

Lohmann, U. and Hoose, C.: Sensitivity studies of different aerosol indirect effects in mixed-phase clouds, Atmos. Chem. Phys., 9, 8917–8934, https://doi.org/10.5194/acp-9-8917-2009, 2009.

Lohmann, U. and Roeckner, E.: Design and performance of a new cloud microphysics scheme developed for the ECHAM general circulation model, Clim. Dynam., 12, 557–572, https://doi.org/10.1007/BF00207939, 1996.

Lohmann, U., Stier, P., Hoose, C., Ferrachat, S., Kloster, S., Roeckner, E., and Zhang, J.: Cloud microphysics and aerosol indirect effects in the global climate model ECHAM5-HAM, Atmos. Chem. Phys., 7, 3425–3446, https://doi.org/10.5194/acp-7-3425-2007, 2007.

Lott, F.: Alleviation of Stationary Biases in a GCM through a Mountain Drag Parameterization Scheme and a Simple Representation of Mountain Lift Forces, Mon. Weather Rev., 127, 788–801, https://doi.org/10.1175/1520-0493(1999)127<0788:AOSBIA>2.0.CO;2, 1999.

Lunt, D. J. and Valdes, P. J.: Dust deposition and provenance at the Last Glacial Maximum and present day, Geophys. Res. Lett., 29, 42-1–42-4, https://doi.org/10.1029/2002GL015656, 2002.

Maher, B., Prospero, J., Mackie, D., Gaiero, D., Hesse, P., and Balkanski, Y.: Global connections between Aeolian dust, climate and ocean biogeochemistry at the present day and at the last glacial maximum, Quaternary Sci. Rev., 28, 2851–2866, https://doi.org/10.1016/j.earscirev.2009.12.001, 2010.

Mahowald, N., Albani, S., Kok, J. F., Engelstaeder, S., Scanza, R., Ward, D. S., and Flanner, M. G.: The size distribution of desert dust aerosols and its impact on the Earth system, Aeolian Res., 15, 53–71, https://doi.org/10.1016/j.aeolia.2013.09.002, 2014.

Mahowald, N. M., Muhs, D. R., Levis, S., Rasch, P. J., Yoshioka, M., Zender, C. S., and Luo, C.: Change in atmospheric mineral aerosols in response to climate: Last glacial period, preindustrial, modern, and doubled carbon dioxide climates, J. Geophys. Res.-Atmos., 111, D10202, https://doi.org/10.1029/2005JD006653, 2006.

Markle, B. R., Steig, E. J., Roe, G. H., Winckler, G., and McConnell, J. R.: Concomitant variability in high-latitude aerosols, water isotopes and the hydrologic cycle, Nat. Geosci., 11, 853–859, https://doi.org/10.1038/s41561-018-0210-9, 2018.

Marticorena, B. and Bergametti, G.: Modeling the atmospheric dust cycle. Part 1: Design of a soil-derived dust emission scheme, J. Geophys. Res., 100, 16415–16430, https://doi.org/10.1029/95JD00690, 1995.

Marticorena, B., Bergametti, G., Aumont, B., Callot, Y., N'Doumé, C., and Legrand, M.: Modeling the atmospheric dust cycle: 2. Simulation of Saharan dust sources, J. Geophys. Res.-Atmos., 102, 4387–4404, https://doi.org/10.1029/96JD02964, 1997.

Martin, J. H.: Glacial-interglacial CO_2 change: The Iron Hypothesis, Paleoceanography, 5, 1–13, https://doi.org/10.1029/PA005i001p00001, 1990.

Martin, J. H., Gordon, R. M., and Fitzwater, S. E.: Iron in Antarctic waters, Nature, 345, 156–158, https://doi.org/10.1038/345156a0, 1990.

Martínez-Garcia, A., Rosell-Melé, A., Jaccard, S. L., Geibert, W., Sigman, D. M., and Haug, G. H.: Southern Ocean dust–climate coupling over the past four million years, Nature, 476, 312–315, https://doi.org/10.1038/nature10310, 2011.

McGee, D., Winckler, G., Borunda, A., Serno, S., Anderson, R., Recasens, C., Bory, A., Gaiero, D., Jaccard, S., Kaplan, M., McManus, J., Revel, M., and Sun, Y.: Tracking eolian dust with helium and thorium: Impacts of grain size and provenance, Geochim. Cosmochim. Ac., 175, 47-67, https://doi.org/10.1016/j.gca.2015.11.023, 2015.

Neubauer, D., Ferrachat, S., Siegenthaler-Le Drian, C., Stier, P., Partridge, D. G., Tegen, I., Bey, I., Stanelle, T., Kokkola, H., and Lohmann, U.: The global aerosol–climate model ECHAM6.3–HAM2.3 – Part 2: Cloud evaluation, aerosol radiative forcing, and climate sensitivity, Geosci. Model Dev., 12, 3609–3639, https://doi.org/10.5194/gmd-12-3609-2019, 2019.

Paul, A. and Schäfer-Neth, C.: Modeling the water masses of the Atlantic Ocean at the Last Glacial Maximum, Paleoceanography, 18, 1058, https://doi.org/10.1029/2002PA000783, 2003.

Ray, N. and Adams, J.: A GIS-based vegetation map of the world at the Last Glacial Maximum (25,000–15,000 BP), Internet Archaeology, 11, https://doi.org/10.11141/ia.11.2, 2001.

Reichholf, J. H.: Is Saharan Dust a Major Source of Nutrients for the Amazonian Rain Forest?, Stud. Neotrop. Fauna E., 21, 251–255, https://doi.org/10.1080/01650528609360710, 1986.

Reick, C. H., Raddatz, T., Brovkin, V., and Gayler, V.: Representation of natural and anthropogenic land cover change in MPI-ESM: Land Cover in MPI-ESM, J. Adv. Model. Earth Sy., 5, 459–482, https://doi.org/10.1002/jame.20022, 2013.

Rojas, M., Moreno, P., Kageyama, M., Crucifix, M., Hewitt, C., Abe-Ouchi, A., Ohgaito, R., Brady, E. C., and Hope, P.: The Southern Westerlies during the last glacial maximum in PMIP2 simulations, Clim. Dynam., 32, 525–548, https://doi.org/10.1007/s00382-008-0421-7, 2009.

Schultz, M. G., Stadtler, S., Schröder, S., Taraborrelli, D., Franco, B., Krefting, J., Henrot, A., Ferrachat, S., Lohmann, U., Neubauer, D., Siegenthaler-Le Drian, C., Wahl, S., Kokkola, H., Kühn, T., Rast, S., Schmidt, H., Stier, P., Kinnison, D., Tyndall, G. S., Orlando, J. J., and Wespes, C.: The chemistry–climate model ECHAM6.3-HAM2.3-MOZ1.0, Geosci. Model Dev., 11, 1695–1723, https://doi.org/10.5194/gmd-11-1695-2018, 2018.

Shao, Y., Wyrwoll, K.-H., Chappell, A., Huang, J., Lin, Z., McTainsh, G. H., Mikami, M., Tanaka, T. Y., Wang, X., and Yoon, S.: Dust cycle: An emerging core theme in Earth system science, Aeolian Res., 2, 181–204, https://doi.org/10.1016/j.aeolia.2011.02.001, 2011.

Sime, L. C., Kohfeld, K. E., Le Quéré, C., Wolff, E. W., de Boer, A. M., Graham, R. M., and Bopp, L.: Southern Hemisphere westerly wind changes during the Last Glacial Maxi-

mum: model-data comparison, Quaternary Sci. Rev., 64, 104–120, https://doi.org/10.1016/j.quascirev.2012.12.008, 2013.

Simmons, A. J. and Jiabin, C.: The calculation of geopotential and the pressure gradient in the ECMWF atmospheric model: Influence on the simulation of the polar atmosphere and on temperature analyses, Q. J. Roy. Meteor. Soc., 117, 29–58, https://doi.org/10.1002/qj.49711749703, 1991.

Simmons, A. J., Burridge, D. M., Jarraud, M., Girard, C., and Wergen, W.: The ECMWF medium-range prediction models development of the numerical formulations and the impact of increased resolution, Meteorol. Atmos. Phys., 40, 28–60, https://doi.org/10.1007/BF01027467, 1989.

Spracklen, D. V., Carslaw, K. S., Kulmala, M., Kerminen, V.-M., Sihto, S.-L., Riipinen, I., Merikanto, J., Mann, G. W., Chipperfield, M. P., Wiedensohler, A., Birmili, W., and Lihavainen, H.: Contribution of particle formation to global cloud condensation nuclei concentrations, Geophys. Res. Lett., 35, L06808, https://doi.org/10.1029/2007GL033038, 2008.

Stanelle, T., Bey, I., Raddatz, T., Reick, C., and Tegen, I.: Anthropogenically induced changes in twentieth century mineral dust burden and the associated impact on radiative forcing, J. Geophys. Res.-Atmos., 119, 13526–13546, https://doi.org/10.1002/2014JD022062, 2014.

Steffensen, J. P.: The size distribution of microparticles from selected segments of the Greenland Ice Core Project ice core representing different climatic periods, J. Geophys. Res.-Oceans, 102, 26755–26763, https://doi.org/10.1029/97JC01490, 1997.

Stevens, B., Giorgetta, M., Esch, M., Mauritsen, T., Crueger, T., Rast, S., Salzmann, M., Schmidt, H., Bader, J., Block, K., Brokopf, R., Fast, I., Kinne, S., Kornblueh, L., Lohmann, U., Pincus, R., Reichler, T., and Roeckner, E.: Atmospheric component of the MPI-M Earth System Model: ECHAM6: ECHAM6, J. Adv. Model. Earth Sy., 5, 146–172, https://doi.org/10.1002/jame.20015, 2013.

Stier, P., Feichter, J., Kinne, S., Kloster, S., Vignati, E., Wilson, J., Ganzeveld, L., Tegen, I., Werner, M., Balkanski, Y., Schulz, M., Boucher, O., Minikin, A., and Petzold, A.: The aerosol-climate model ECHAM5-HAM, Atmos. Chem. Phys., 5, 1125–1156, https://doi.org/10.5194/acp-5-1125-2005, 2005.

Sundqvist, H., Berge, E., and Kristjánsson, J. E.: Condensation and Cloud Parameterization Studies with a Mesoscale Numerical Weather Prediction Model, Mon. Weather Rev., 117, 1641, https://doi.org/10.1175/1520-0493(1989)117<1641:CACPSW>2.0.CO;2, 1989.

Takemura, T., Egashira, M., Matsuzawa, K., Ichijo, H., O'ishi, R., and Abe-Ouchi, A.: A simulation of the global distribution and radiative forcing of soil dust aerosols at the Last Glacial Maximum, Atmos. Chem. Phys., 9, 3061–3073, https://doi.org/10.5194/acp-9-3061-2009, 2009.

Taylor, K., Williamson, D., and Zwiers, F.: AMIP II Sea Surface Temperature and Sea Ice Concentration Boundary Conditions, Program for Climate Model Diagnosis and Intercomparison, University of California, Lawrence Livermore National Laboratory, PCMDI Rep, 60, 2000.

Tegen, I. and Fung, I.: Modeling of mineral dust in the atmosphere: Sources, transport, and optical thickness, J. Geophys. Res.-Atmos., 99, 22897–22914, https://doi.org/10.1029/94JD01928, 1994.

Tegen, I., Neubauer, D., Ferrachat, S., Siegenthaler-Le Drian, C., Bey, I., Schutgens, N., Stier, P., Watson-Parris, D., Stanelle, T., Schmidt, H., Rast, S., Kokkola, H., Schultz, M., Schroeder, S., Daskalakis, N., Barthel, S., Heinold, B., and Lohmann, U.: The global aerosol–climate model ECHAM6.3–HAM2.3 – Part 1: Aerosol evaluation, Geosci. Model Dev., 12, 1643–1677, https://doi.org/10.5194/gmd-12-1643-2019, 2019.

Tierney, J. E., Zhu, J., King, J., Malevich, S. B., Hakim, G. J., and Poulsen, C. J.: Glacial cooling and climate sensitivity revisited, Nature, 584, 569–573, https://doi.org/10.1038/s41586-020-2617-x, 2020.

Vallelonga, P.: The enigma of dust provenance: where else does Antarctic dust come from?, Past Global Changes Magazine, 22, 74–75, https://doi.org/10.22498/pages.22.2.74, 2014.

van der Does, M., Wengler, M., Lamy, F., Martínez-García, A., Jaccard, S. L., Kuhn, G., Lanny, V., Stuut, J.-B. W., and Winckler, G.: Opposite dust grain-size patterns in the Pacific and Atlantic sectors of the Southern Ocean during the last 260,000 years, Quaternary Sci. Rev., 263, 106978, https://doi.org/10.1016/j.quascirev.2021.106978, 2021.

Vignati, E., Wilson, J., and Stier, P.: M7: An efficient size-resolved aerosol microphysics module for large-scale aerosol transport models, J. Geophys. Res.-Atmos., 109, D22202, https://doi.org/10.1029/2003JD004485, 2004.

Werner, M., Tegen, I., Harrison, S. P., Kohfeld, K. E., Prentice, I. C., Balkanski, Y., Rodhe, H., and Roelandt, C.: Seasonal and interannual variability of the mineral dust cycle under present and glacial climate conditions, J. Geophys. Res.-Atmos., 107, AAC2-1–AAC2-19, https://doi.org/10.1029/2002JD002365, 2002.

White, B. R.: soil transport by winds on Mars, J. Geophys. Res.-Sol. Ea., 84, 4643–4651, https://doi.org/10.1029/JB084iB09p04643, 1979.

Wilson, J., Cuvelier, C., and Raes, F.: A modeling study of global mixed aerosol fields, J. Geophys. Res.-Atmos., 106, 34081–34108, https://doi.org/10.1029/2000JD000198, 2001.

Wolff, E. W., Barbante, C., Becagli, S., Bigler, M., Boutron, C. F., Castellano, E., de Angelis, M., Federer, U., Fischer, H., Fundel, F., Hansson, M., Hutterli, M., Jonsell, U., Karlin, T., Kaufmann, P., Lambert, F., Littot, G. C., Mulvaney, R., Röthlisberger, R., Ruth, U., Severi, M., Siggaard-Andersen, M. L., Sime, L. C., Steffensen, J. P., Stocker, T. F., Traversi, R., Twarloh, B., Udisti, R., Wagenbach, D., and Wegner, A.: Changes in environment over the last 800,000 years from chemical analysis of the EPICA Dome C ice core, Quaternary Sci. Rev., 29, 285–295, https://doi.org/10.1016/j.quascirev.2009.06.013, 2010.